nature communications

Article

https://doi.org/10.1038/s41467-024-53038-2

Distinctive CD39$^+$CD9$^+$ lung interstitial macrophages suppress IL-23/Th17-mediated neutrophilic asthma by inhibiting NETosis

Received: 4 June 2023

Accepted: 30 September 2024

Published online: 04 October 2024

Check for updates

Seunghan Han[1,2,13], Bomin Kim[1,2,13], Do Young Hyeon[3,13], Daeun Jeong[1,2], Jaechan Ryu[4], Jae-Sung Nam[5], Yoon Ha Choi[6], Bo-Ram Kim[2,7], Sang Chul Park[8], Youn Wook Chung[1,2], Sung Jae Shin[2,7,9], June-Yong Lee[2,7,9], Jong Kyoung Kim[6], Jihye Park[10], Sei Won Lee[11], Tae-Bum Kim[12], Jae Hee Cheon[10], Hyung-Ju Cho[5], Chang-Hoon Kim[5], Joo-Heon Yoon[5] ✉, Daehee Hwang[3] ✉ & Ji-Hwan Ryu[1,2] ✉

The IL-23-Th17 axis is responsible for neutrophilic inflammation in various inflammatory diseases. Here, we discover a potential pathway to inhibit neutrophilic asthma. In our neutrophil-dominant asthma (NDA) model, single-cell RNA-seq analysis identifies a subpopulation of CD39$^+$CD9$^+$ interstitial macrophages (IMs) suppressed by IL-23 in NDA conditions but increased by an IL-23 inhibitor αIL-23p19. Adoptively transferred CD39$^+$CD9$^+$ IMs suppress neutrophil extracellular trap formation (NETosis), a representative phenotype of NDA, and also Th17 cell activation and neutrophilic inflammation. CD39$^+$CD9$^+$ IMs first attach to neutrophils in a CD9-dependent manner, and then remove ATP near neutrophils that contribute to NETosis in a CD39-dependent manner. Transcriptomic data from asthmatic patients finally show decreased CD39$^+$CD9$^+$ IMs in severe asthma than mild/moderate asthma. Our results suggest that CD39$^+$CD9$^+$ IMs function as a potent negative regulator of neutrophilic inflammation by suppressing NETosis in the IL-23-Th17 axis and can thus serve as a potential therapeutic target for IL-23-Th17-mediated neutrophilic asthma.

Asthma is a chronic inflammatory disorder of the airways with high morbidity[1–3]. There are several types of asthmatic airway inflammation involving Th2 cell-mediated eosinophilic, Th17 cell-mediated neutrophilic, or even agranulocytic inflammation[4]. Relationships of lung neutrophilic inflammation with severity and exacerbations in asthma have been reported in patients[5,6]. Neutrophilic airway inflammation often shows no response to inhaled or systemic corticosteroids, unlike eosinophilic airway inflammation, resulting in poor disease control

[1]Department of Biomedical Sciences, Yonsei University College of Medicine, Seoul, Korea. [2]Brain Korea 21 PLUS Project for Medical Science, Yonsei University College of Medicine, Seoul, Korea. [3]School of Biological Sciences, Seoul National University, Seoul, Korea. [4]Institut Pasteur, Microenvironment and Immunity Unit, Paris, France. [5]Department of Otorhinolaryngology and Airway Mucus Institute, Yonsei University College of Medicine, Seoul, Korea. [6]Department of Life Sciences, Pohang University of Science and Technology, Pohang, Korea. [7]Department of Microbiology and Immunology, Yonsei University College of Medicine, Seoul, Korea. [8]Department of Otorhinolaryngology–Head and Neck Surgery, Kangnam Sacred Heart Hospital, Hallym University College of Medicine, Seoul, Korea. [9]Institute for Immunology and Immunological Diseases, Yonsei University College of Medicine, Seoul, Korea. [10]Department of Internal Medicine, Yonsei University College of Medicine, Seoul, Korea. [11]Department of Pulmonary and Critical Care Medicine, Asan Medical Center, University of Ulsan College of Medicine, Seoul, Korea. [12]Department of Allergy and Clinical Immunology, Asan Medical Center, University of Ulsan College of Medicine, Seoul, Korea. [13]These authors contributed equally: Seunghan Han, Bomin Kim, Do Young Hyeon. ✉e-mail: jhyoon@yuhs.ac; daehee@snu.ac.kr; yjh@yuhs.ac

and recurrent exacerbations[7]. Therefore, there has been a significant need for alternative therapeutic approaches for neutrophilic airway inflammation[8]. However, the development of a new therapy suited for neutrophilic asthma has been hampered because of a limited understanding of the underlying mechanisms[9].

Myeloid cells, including macrophages and dendritic cells (DCs), have antigen-presenting roles, instruct naïve $CD4^+$ T cell differentiation into effector Th2 and Th17 cells in asthma, and control tolerance to inhaled antigens[10,11]. High doses of antigens, such as ovalbumin (OVA) and house dust mite (HDM), coupled with lipopolysaccharide (LPS) stimulation are reported to induce Th17 cell differentiation, involving expression of CD40 and CD86, and high levels of pro-inflammatory cytokines, including IL-6, IL-1β, IL-23, and transforming growth factor-β (TGF-β)[12–15]. In particular, IL-23 induces neutrophilic infiltration in the airways of asthmatic mice, leading to neutrophilic asthma through Th17 cell activation and IL-17 secretion[16,17]. Recently, potential therapeutic effects of IL-23 inhibition using IL-23 antagonists or by depletion of IL-23 have been evaluated in patients with neutrophilic asthma or mouse models with neutrophil-dominant asthma (NDA)[18–20]. However, the development of IL-23-targeting therapeutics has been slowed down because the regulatory mechanisms of IL-23 and its specific role in neutrophilic asthma are not clear. Thus, the target cells of IL-23 and their functional roles in neutrophilic inflammation need to be investigated.

In response to infectious stimuli, neutrophils form neutrophil extracellular traps (NETs) to protect the host[21,22], yet these structures also mediate tissue injury and inflammation[23–25]. NETs contain double-stranded DNA (dsDNA) and modified histone proteins, such as citrullinated histone H3 (Cit-H3), and granule proteins, including neutrophil elastase (NE) and myeloperoxidase (MPO)[26]. Increased neutrophils during severe asthma can lead to the formation of NETs, called NETosis[27–29]. Host dsDNA released by NETosis stimulates rhinovirus-induced allergic asthma exacerbation[30], and low-dose LPS-induced NETosis promotes allergic airway inflammation in response to HDM[31].

To identify cell populations associated with various lung disease conditions, single-cell RNA-sequencing (scRNA-seq) has been commonly employed[32–35]. The lung is a multifaceted tissue composed of more than 40 kinds of cell populations[36]. A few single-cell analyses have been performed for respiratory diseases. For example, scRNA-seq analysis in mouse models has reconstructed cell lineage hierarchies of lung epithelial cells and identified further subsets of innate lymphoid cell (ILC) precursors[37–39]. It was also applied to decipher subpopulations of lung-resident ILCs in a mouse model with HDM-driven inflammation, and type 2 ILC2s expressing the neuromedin U (NMU) receptor (NMUR) were found as a key subpopulation to modulate inflammatory responses to HDM[40]. However, the target cells of IL-23 in neutrophilic inflammation have not been investigated using scRNA-seq analysis.

Here, we focus on $CD39^+CD9^+$ interstitial macrophages (IMs), identified through scRNA-seq analysis, and demonstrate their functional roles in neutrophilic asthma. Using molecular and cellular experiments in OVA- and HDM-driven mouse models, we show that $CD39^+CD9^+$ IMs are crucial in alleviating neutrophilic inflammation and reducing airway responses. Our findings highlight the importance of these macrophage subsets in modulating the pathogenesis of neutrophilic asthma, offering potential therapeutic targets for managing severe asthma phenotypes.

Results

IL-23 inhibitor suppresses the development of Th17-mediated neutrophilic inflammation in NDA mouse lungs

To establish the OVA-driven NDA model, mice were sensitized to OVA (75 μg) and LPS (10 μg) on days 0, 1, 2, and 7. Mice were then challenged with only OVA (100 μg) on days 14, 15, 21, and 22 sacrificed on day 24[41]. The sensitization/challenge scheme is summarized in Fig. 1a. Total cell, neutrophil, and eosinophil counts in the bronchoalveolar lavage fluid (BALF) were significantly increased in OVA + LPS/OVA compared to in phosphate-buffered saline (PBS)/PBS or OVA + LPS/PBS (Fig. 1b).

We next determined which T helper (Th) cells were predominantly activated in OVA + LPS/OVA through fluorescence-activated cell sorting (FACS) analysis using antibodies against RORγt (Th17), T-bet (Th1), and GATA3 (Th2) (Supplementary Fig. 1a). Although all three types of Th cells were increased in OVA + LPS/OVA compared to in PBS/PBS or OVA + LPS/PBS, the increase of $ROR\gamma t^+$ Th17 cells (~6.0×10^4 cells) was much higher than those of $T\text{-}bet^+$ Th1 (~1.5×10^4) and $GATA3^+$ Th2 cells (~2×10^3) (Fig. 1c). Correspondingly, the Th17-related cytokine IL-17 was significantly increased in OVA + LPS/OVA compared to in PBS/PBS or OVA + LPS/PBS (Fig. 1d). Cytokines related to Th1 (IFN-γ) and Th2 (IL-13) cells were also increased, consistent with the increased $T\text{-}bet^+$ and $GATA3^+$ Th cells (Fig. 1d). Moreover, hematoxylin and eosin (H&E)-stained lung sections showed the increased immune cell recruitment into lung tissue in OVA + LPS/OVA, compared to that in PBS/PBS or OVA + LPS/PBS (Fig. 1e, f). Periodic acid–Schiff (PAS) staining also showed a similar increase of goblet cell hyperplasia (Fig. 1g, h). Furthermore, both enhanced pause P_{enh} (Fig. 1i) and respiratory resistance R_{rs} values (Fig. 1j) were significantly higher, suggesting worse respiratory functions in OVA + LPS/OVA than in PBS/PBS or OVA + LPS/PBS.

Next, we investigated the effects of Dexamethasone (Dex), a corticosteroid medication, on attenuation in our NDA model (Fig. 1a). Dex administration had no significant effect on the increased counts of total cells and neutrophils in BALF, and $ROR\gamma t^+$ and $T\text{-}bet^+$ Th cells in lung tissues in OVA + LPS/OVA, but attenuated eosinophils and $GATA3^+$ Th cells (Fig. 1b, c). Dex administration led to no changes in the increased IL-17 in OVA + LPS/OVA but attenuated the increase of IFN-γ and IL-13 (Fig. 1d). Of note, the alteration pattern of IFN-γ was found to be inconsistent with that of $T\text{-}bet^+$ Th cells after Dex administration, indicating that IFN-γ is not entirely specific to $T\text{-}bet^+$ Th cells, which may also explain its unexpected higher level in OVA + LPS/OVA (Fig. 1d). Immune cell infiltration (Fig. 1e, f), goblet cell hyperplasia (Fig. 1g, h), and P_{enh} (Fig. 1i) and R_{rs} values (Fig. 1j) were also not attenuated by Dex administration. These results indicate that Dex fails to reduce Th17 activation and neutrophilic inflammation in our NDA mice.

IL-23 cytokine secreted from inflammatory DCs is critical for Th17 activation[16]. To test the contribution of IL-23 to Th17 activation and neutrophilic inflammation in NDA mice, we treated NDA mice with αIL-23p19 (Fig. 1a). αIL-23p19 administration significantly reduced the increased BALF total cell, neutrophil, and eosinophil counts in OVA + LPS/OVA (Fig. 1b), and also attenuated the increased $ROR\gamma t^+$, $T\text{-}bet^+$, and $GATA3^+$ Th cells and levels of their cytokines (Fig. 1c, d), as well as the increased immune cell infiltration, goblet cell hyperplasia and P_{enh} and R_{rs} values (Fig. 1e–j). These results indicate that IL-23 is required for Th17 activation, neutrophilic inflammation, and pathophysiology in OVA + LPS/OVA. Of note, the levels of TNF and IL-6, known to be associated with severe asthma[42], were also increased in OVA + LPS/OVA, which was significantly reduced by αIL-23p19 administration (Supplementary Fig. 1b).

We next attempted to confirm the above findings in HDM-driven asthma models established using the previously reported intranasal sensitization (HDM + LPS) and challenge (HDM) protocol[43] (Supplementary Fig. 2a). Of note, we used HDM + LPS/PBS only in this HDM model as a control because PBS/PBS control always showed weaker levels of all the measures that OVA + LPS/PBS control in the OVA model. Consistent with the findings from the OVA models, total cell, neutrophil, and eosinophil counts in BALF were significantly increased in HDM + LPS/HDM compared to in HDM + LPS/PBS (Supplementary Fig. 2b). $ROR\gamma t^+$ Th cell count (~8×10^4) was also much higher than those of $T\text{-}bet^+$ Th cells (~1×10^4), and $GATA3^+$ Th cells (~1.2×10^4) in HDM + LPS/HDM (Supplementary Fig. 2c). Moreover, IL-17, IFN-γ, and

https://doi.org/10.1038/s41467-024-53038-2

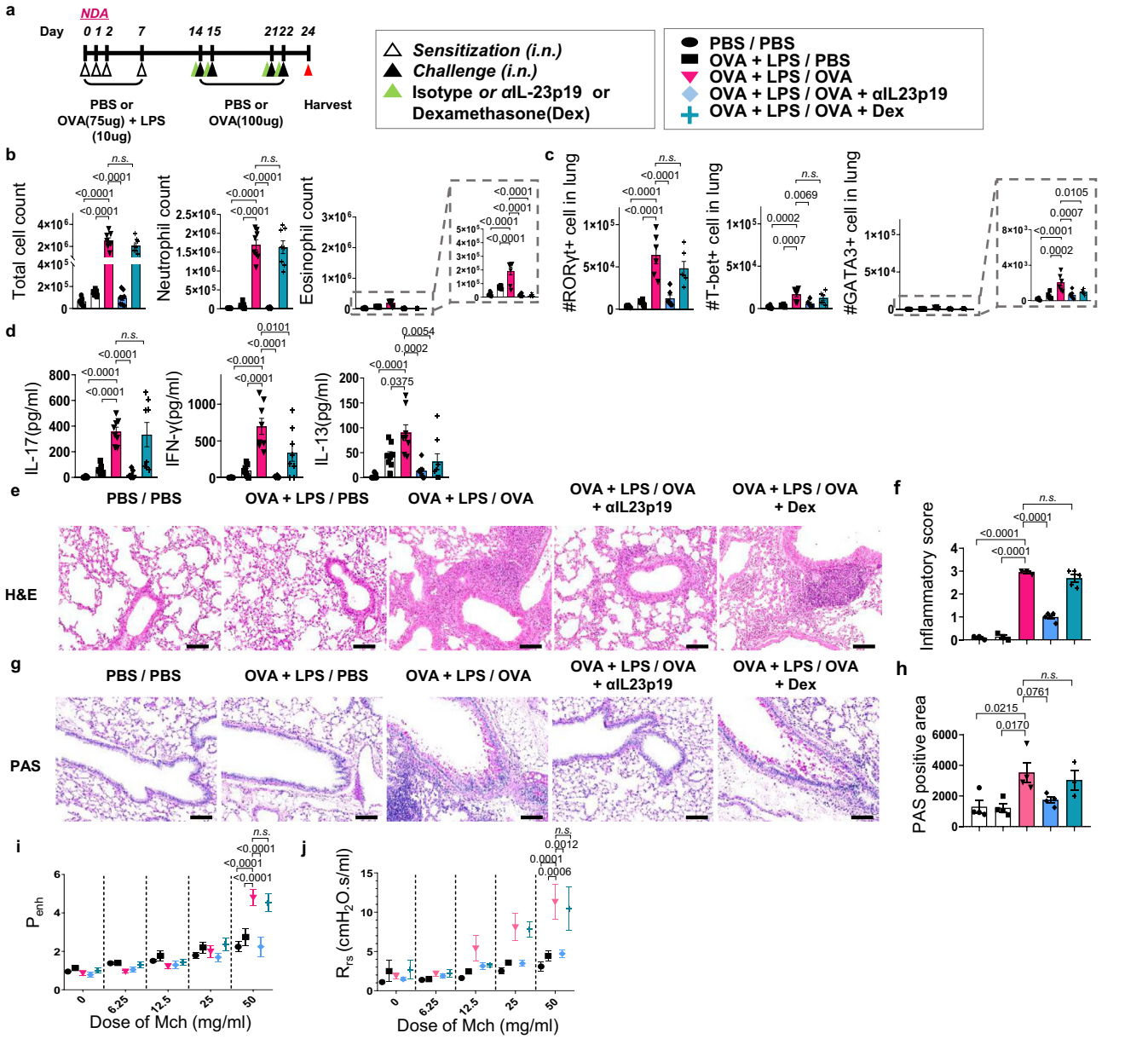

Fig. 1 | IL-23 inhibitor suppresses the development of Th17-mediated neutrophilic inflammation in NDA mice. a Schematic diagram of allergen sensitization and challenge protocol. In the NDA mouse model, sensitization with PBS or OVA + LPS intranasally (*i.n.*) was followed by challenge with PBS or OVA (*i.n.*) at the indicated days. Isotype control, αIL-23p19, or dexamethasone (Dex), was treated at 1 hr before every challenge period. The inflammatory response was assessed at 48 hr after the last challenge. **b** Total cell, neutrophil, and eosinophil counts in BALF measured using flow ($n = 8$ mice per group). **c** RORγt$^+$, T-bet$^+$, and GATA3$^+$ Th cell counts in CD4$^+$ T cells (Live,Dump$^-$FOXP3$^-$CD44$^+$CD4$^+$TCRb$^+$) measured using flow cytometry ($n = 6$ mice per group). **d** Levels of Th17 (IL-17), Th1 (IFN-γ), and Th2 (IL-13) cell-related cytokine in BALF ($n = 8$ mice per group). **e** Representative H&E staining of lung sections obtained from the indicated conditions. Scale bar = 100 μm. **f** Inflammatory scores quantified from H&E staining (PBS/PBS ($n = 3$), OVA + LPS/PBS ($n = 3$), OVA + LPS/OVA ($n = 3$), OVA + LPS/OVA + αIL-23p19 ($n = 5$), and OVA + LPS/OVA+Dex ($n = 5$)). **g** Representative PAS staining of lung sections obtained from the indicated conditions. Scale bar = 200 μm. **h** PAS-positive area quantified from PAS staining ($n = 4$ mice per group) (**i**)P_{enh} values measured using whole body plethysmography (PBS/PBS ($n = 8$), OVA + LPS/PBS ($n = 9$), OVA + LPS/OVA ($n = 8$), OVA + LPS/OVA + αIL-23p19 ($n = 5$), and OVA + LPS/OVA +Dex ($n = 8$)). **j** R_{rs} values measured using an invasive ventilated lung resistance method (PBS/PBS ($n = 3$), OVA + LPS/PBS ($n = 4$), OVA + LPS/OVA ($n = 5$), OVA + LPS/OVA + αIL-23p19 ($n = 4$), and OVA + LPS/OVA + Dex ($n = 5$)). Data are shown as mean ± s.e.m. Significance was determined by one-way analysis of variance (ANOVA) with Tukey's post hoc correction (**b**–**d**, **f**, **h**) and two-way ANOVA with Sidak's post hoc correction (**i**, **j**).

IL-13 levels in BALF, as well as immune cell infiltration, goblet cell hyperplasia, and P_{enh} values (Supplementary Fig. 2d–i), showed the same patterns with those in the OVA model. All these increases were reduced by αIL-23p19 (Supplementary Fig. 2b–i). As in the OVA model, Dex administration had no significant effect on the increased counts of total cells and neutrophils in BALF, RORγt$^+$, and T-bet$^+$ Th cells in HDM + LPS/HDM, but attenuated eosinophils and GATA3$^+$ Th cells (Supplementary Fig. 2b, c), and led to no significant changes in the increased IL-17 (Supplementary Fig. 2d). Interestingly, however, Dex administration also showed no effects on IFN-γ, and IL-13 in HDM + LPS/HDM (Supplementary Fig. 2d), which of the latter was inconsistent with the reduced GATA3$^+$ Th cells, suggesting that the cytokines may not reflect well their associated Th cell counts as in the case of IFN-γ in the OVA model.

In our NDA model, αIL-23p19 or Dex was administrated (pre-challenge) 1 h before the OVA challenge at days 14, 15, 21, and 22 (Fig. 1a). In this setting, it is not clear 1) whether the mice have already inflammation at day 14 after the sensitization and αIL-23p19 also suppresses this established inflammation; and 2) whether administration of αIL-23p19 before and after the OVA challenge would make differences in its inhibitory effect. To address these issues, we first evaluated the extent of inflammation at day 14 with PBS (control) or OVA + LPS sensitization alone (Supplementary Fig. 3a). The inflammation was significantly lower in OVA + LPS at day 14 than in OVA + LPS/OVA at day 24, as indicated by the lower BALF total cell, neutrophil, and eosinophil counts (Supplementary Fig. 3b). Furthermore, OVA + LPS sensitization induced no significant differences in the BALF cell counts from PBS sensitization at day 14. Similar patterns were observed for T-bet$^+$ and GATA3$^+$ Th cell counts, IL-17 level, and inflammatory score (Supplementary Fig. 3c–f). These data suggest that the inflammation induced by OVA + LPS sensitization returned to the basal level at day 14. We next administered αIL-23p19 or Dex in 12 h (post-challenge) after the challenge (Supplementary Fig. 4a). The post-challenge administration of αIL-23p19 reduced neutrophilic inflammation and Th17 activation in OVA + LPS/OVA as much effectively as the pre-challenge administration (Supplementary Fig. 4b, c). These data suggest that αIL-23p19 suppresses the inflammation developed during the challenge, regardless of the pre-and post-challenge administration of αIL-23p19. DEX did not rescue the phenotypes of neutrophilic asthma in both pre-and post-challenge models (Supplementary Fig. 4b–g).

Both OVA and HDM models revealed that Th17 cell activation was mixed with Th1 and Th2 cell activation. However, strong Th17 cell activation was consistently observed in both models, while Th1 and Th2 cell activation was relatively weaker with the inconsistency between cytokines and cell counts after Dex administration, suggesting that neutrophil inflammation is mainly driven by Th17 cell activation. To further verify this, we next inhibited the effect of Th17 cell activation by IL-17 neutralizing antibody (αIL-17) administration in OVA + LPS/OVA. αIL-17 administration significantly reduced the increased total cells, neutrophils and cytokine (IL-17, IL-22, and IFN-γ) levels in BALF and RORγt$^+$, T-bet$^+$ T cells, as well as the increased immune cell infiltration in lung and P_{enh} values (Supplementary Fig. 5a–f), in OVA + LPS/OVA, thus supporting the major role of Th17 cells in neutrophilic inflammation in the NDA model.

Single-cell RNA-seq analyses identify myeloid cell subpopulations associated with the inhibitory effect of αIL-23p19 in NDA mouse lungs

To identify immune cell populations associated with the aforementioned inhibitory effects of αIL-23p19, we performed scRNA-seq analysis of CD45$^+$ cells isolated from NDA mouse lungs in OVA + LPS/PBS ($n = 3$), OVA + LPS/OVA ($n = 3$), and OVA + LPS/OVA + αIL-23p19 ($n = 3$). A total of 62,946 cells were selected from these three conditions based on previously reported criteria[44] (Supplementary Fig. 6a, b). Using the transcriptome data of the selected cells after batch correction, we identified 11 cell clusters using Louvain clustering (Fig. 2a). After confirming no bias of each cluster toward a particular condition (Supplementary Fig. 6c and Supplementary Data 1), we then identified marker genes significantly ($P < 0.01$) upregulated in each cluster, with respect to the other clusters, to examine functional characteristics of the cluster (Supplementary Fig. 6d and Supplementary Data 2). We next annotated cell types for these clusters using the SingleR label transfer method[45] with the ImmGen reference dataset[46] (Fig. 2a and Supplementary Fig. 6e, f) and confirmed the cell type annotation using the known marker genes upregulated in each cluster (Fig. 2b and Supplementary Data 3): For example, *C1QB* and *ITGAM* for CD11b$^+$ macrophage (CM); *EAR1* for alveolar macrophage (AM); *CCL17* for dendritic cell (DC); *S100A9* and *CD14* for neutrophil-like cells (NL); *TREML4* for monocyte (MO); *CD79A* for B cell; and *CD3D* and *CTLA4* for T and Treg cells, respectively.

In neutrophilic asthma, diverse myeloid cells are co-recruited into the airways and interplay to promote Th17 cell activation and neutrophil infiltration[47]. To identify the cells associated with the inhibitory effects of αIL-23p19, we thus focused on five myeloid cell clusters (CM, AM, DC, NL, and MO). We then examined the proportions of each cell type originating from the three conditions and found no cell type whose proportions were relatively higher in OVA + LPS/PBS and OVA + LPS/OVA + αIL-23p19 compared to in OVA + LPS/OVA, suggesting no clear associations of the five cell types with the inhibitory effects of αIL-23p19 (Fig. 2c). Since only a subset of cells in each cluster might be associated with the effects of αIL-23p19, we next identified subclusters of these clusters and marker genes upregulated in each subcluster (Fig. 2d, Supplementary Fig. 7a–f and Supplementary Data 4) and annotated these subclusters using their representative marker genes (Supplementary Fig. 7g–k). As potential candidates associated with the inhibitory effects of αIL-23p19, we then selected the following subclusters where the proportions were significantly ($P < 0.05$) reduced in OVA + LPS/OVA compared to in OVA + LPS/PBS and the reduced proportions tended to restore in OVA + LPS/OVA + αIL-23p19 (Fig. 2e): TREM2^{high} CM, circulating NL, non-classical MO, CD36^{high} tissue-resident AM, and classical DC1.

Rather than selecting the best subcluster from these candidates based on any quantitative measures, we integrated the functional characteristics of the candidates independent of their proportions. To evaluate the functional associations of the five candidates with neutrophilic inflammation, we examined cellular pathways represented by the marker genes for each subcluster. Based on these pathways, among the subclusters, we further selected TREM2^{high} CM and circulating NL strongly associated with neutrophil migration/chemotaxis, a representative cellular process for neutrophilic inflammation (Fig. 2f). Finally, for the subsequent functional studies of TREM2^{high} CM and circulating NL, among their marker genes, we selected the ones whose proteins are localized on plasma membrane for their isolation using FACS and also that had anti-inflammatory functions for associations with the inhibitory effects of αIL-23p19. We then prioritized the merged set of the selected marker genes for TREM2^{high} CM and circulating NL based on the mean percentage of cells expressing each marker gene in the two subclusters (Fig. 2g). Among the top genes, we finally selected CD9, a known anti-inflammatory adhesion molecule[48], and CD39, an ATPase inhibiting ATP-dependent inflammation[49].

Myeloid cells expanded by αIL-23p19 administration are Ly6G$^-$ negative CD39$^+$CD9$^+$ interstitial macrophages

The above results suggest that myeloid cell subpopulations (TREM2^{high} CM and circulating NL) expressing the anti-inflammatory genes *CD39* and *CD9* are potentially associated with the inhibitory effects of αIL-23p19. To test this finding, we gated CD45$^+$CD11b$^+$CD11c$^-$ cells isolated from NDA mouse lungs into Ly6G$^-$ and Ly6G$^+$ (neutrophils) cells and further into Ly6G$^-$CD39$^+$CD9$^+$CD11b$^+$CD11c$^-$ and Ly6G$^+$CD39$^+$CD9$^+$CD11b$^+$CD11c$^-$ cells, which are considered to correspond to TREM2^{high} CM and circulating NL, respectively (Supplementary Fig. 8a, b). The percentages of Ly6G$^+$CD11b$^+$CD11c$^-$ neutrophils were increased in OVA + LPS/OVA in the lung, and such increase was reduced by αIL-23p19 (Fig. 3a), confirming the findings from BALF (Fig. 1b). The percentage of Ly6G$^-$CD39$^+$CD9$^+$CD11b$^+$CD11c$^-$ cells was decreased significantly in OVA + LPS/OVA compared to in OVA + LPS/PBS, which was restored in OVA + LPS/OVA + αIL-23p19 (Fig. 3b). In contrast, the percentage of Ly6G$^+$CD39$^+$CD9$^+$CD11b$^+$CD11c$^-$ cells were not significantly different between OVA + LPS/OVA and OVA + LPS/OVA + αIL-23p19 (Fig. 3c). We further performed bulk RNA-seq analysis ($n = 3$) of Ly6G$^-$CD39$^+$CD9$^+$CD11b$^+$CD11c$^-$ cells sorted from OVA + LPS/OVA + αIL-23p19 using FACS. With the bulk data, we then estimated fractions of CM subclusters using CIBERSORTx[50] and found that TREM2^{high}

https://doi.org/10.1038/s41467-024-53038-2

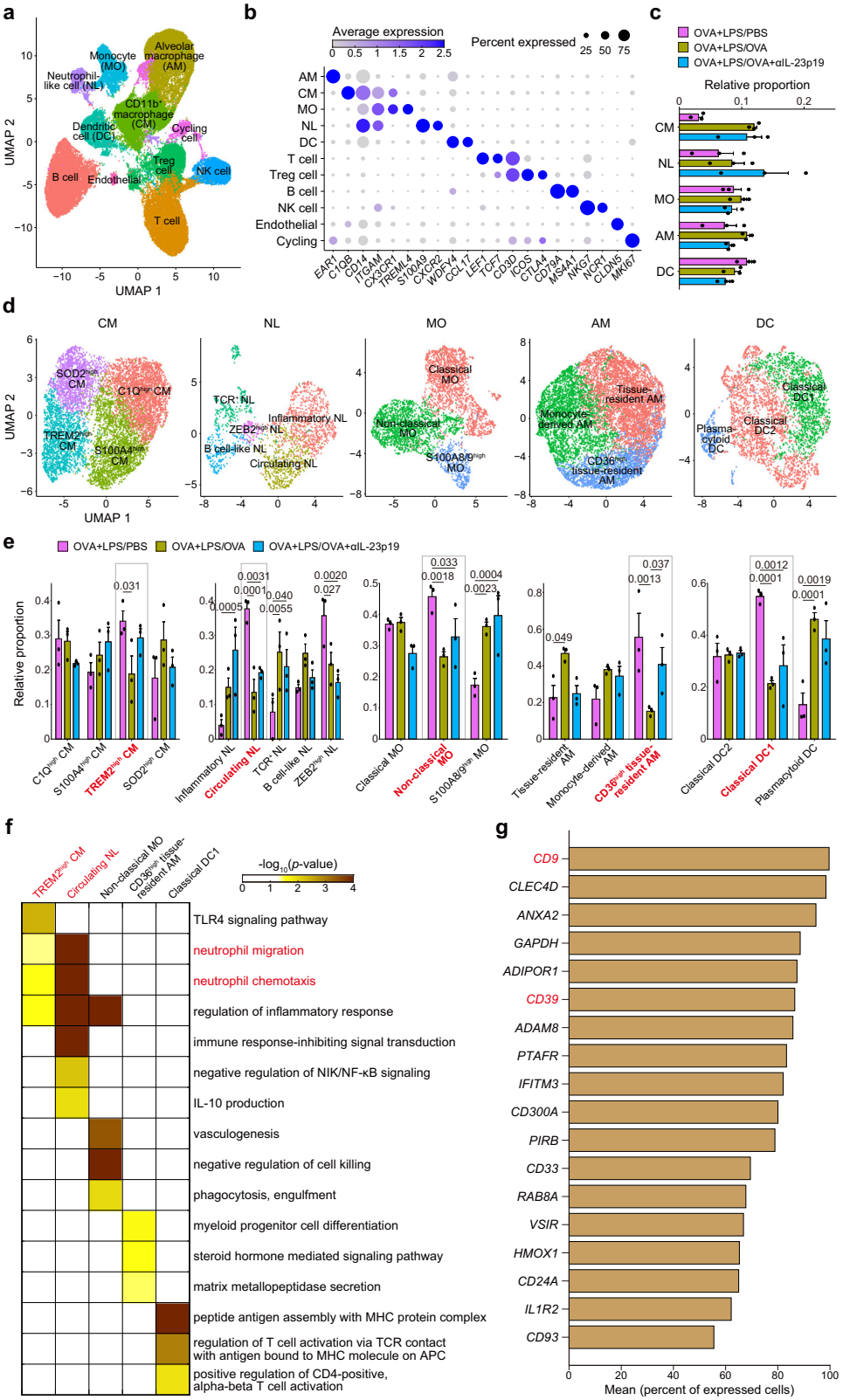

CMs were the most highly enriched in the sorted Ly6G$^-$CD39$^+$CD9$^+$ CD11b$^+$CD11c$^-$ cells, compared to the other CM subclusters (Fig. 3d). These data suggest that Ly6G$^-$CD39$^+$CD9$^+$CD11b$^+$CD11c$^-$ cells (TREM2^{high} CM) showed a strong association with the inhibitory effects of αIL-23p19.

To explore the identity of these cells, we examined their morphology by cytospin preparation. The majority of Ly6G$^-$CD39$^+$CD9$^+$ CD11b$^+$CD11c$^-$ cells (94.2%) and Ly6G$^+$CD39$^+$CD9$^+$CD11b$^+$ CD11c$^-$ (90.1%) were mononuclear (MN) and polymorphonuclear (PMN) cells, respectively (Fig. 3e). Given the annotation of TREM2^{high} CM based on scRNA-seq data, we further tested whether the Ly6G$^-$CD39$^+$ CD9$^+$CD11b$^+$CD11c$^-$ cells would be interstitial macrophages (IMs) or other cells (monocytes or CD11b$^+$ DCs). To this end, we gated Ly6G$^-$CD39$^+$CD9$^+$CD11b$^+$CD11c$^-$ and Ly6G$^-$CD39$^-$CD9$^-$CD11b$^+$CD11c$^-$ cells

Fig. 2 | Myeloid cell subpopulations expressing anti-inflammatory genes were increased by αIL-23p19 administration in NDA mouse lungs. a Uniform manifold approximation and projection (UMAP) plot showing 11 clusters of CD45$^+$ immune cells. **b** Dot plot showing relative expression of known marker genes of immune cells (*x*-axis) across all clusters (*y*-axis) (Supplementary Data 3). The color and diameter of the dots indicate the average expression of the indicated gene and the proportion of cells expressing the gene in each cluster, respectively. **c** Relative proportions of cells originated from three conditions in the five myeloid cell clusters. Proportions per cluster in each sample were normalized for their sum to be one. **d** UMAP plots showing subclusters of the indicated myeloid cell clusters. **e** Relative proportions of cells originated from three conditions in the subclusters of the indicated myeloid cell clusters. Red highlighted clusters with higher proportions of the cells in OVA + LPS/OVA + αIL-23p19 (P19) and OVA + LPS/PBS (PBS) than those in OVA + LPS/OVA (OVA). Proportions per cluster in each sample were normalized for their sum to be one. **f** Heat map showing gene ontology biological processes (GOBPs) enriched by marker genes for the five selected subclusters and their enrichment significance (p) from the DAVID software as $-\log_{10}(p\text{-value})$. Red labeled, GOBPs related to neutrophilic inflammation and subclusters in which those GOBPs are enriched. **g** Bar plot showing the mean percentage of cells expressing the indicated anti-inflammatory genes whose proteins are localized on the plasma membrane in TREM2^{high} CM and Circulating NL. Red labeled, candidate genes associated with the inhibitory effects of αIL-23p19. (**a**–**g**) $n = 3$ samples. Data are shown as mean ± s.e.m. Significance was determined by two-way ANOVA with Tukey's post hoc correction (**e**).

using the expression of F4/80 and MHC class II (MHCII)[51] and found that Ly6G$^-$CD39$^+$CD9$^+$CD11b$^+$CD11c$^-$ cells showed higher expression of both F4/80 and MHCII in OVA + LPS/OVA + αIL-23p19 than Ly6G$^-$CD39$^-$CD9$^-$CD11b$^+$CD11c$^-$ cells (Fig. 3f). Taken together, these results indicate that Ly6G$^-$CD39$^+$CD9$^+$CD11b$^+$CD11c$^-$ cells are CD39$^+$CD9$^+$ IMs while Ly6G$^-$CD39$^-$CD9$^-$CD11b$^+$CD11c$^-$ cells are CD39$^-$CD9$^-$ monocytes.

Previously, IL-10-producing IMs were reported to inhibit allergen-induced neutrophilic asthma by inhibiting Th2 and Th17 responses[51]. However, in the lung of our NDA model, IL-10-producing CD39$^+$CD9$^+$ IMs were not detected in OVA + LPS/PBS or OVA + LPS/OVA + αIL-23p19 (Fig. 3g), and IL-10 levels in BALF were not changed by αIL-23p19 (Fig. 3h), indicating that CD39$^+$CD9$^+$ IMs function in an IL-10-independent manner. To examine how the increased IL-23 leads to a decrease in the CD39$^+$CD9$^+$ IMs population, we hypothesized that the IL-23 increase in NDA condition could induce cell death of CD39$^+$CD9$^+$ IMs. To test this hypothesis, we obtained CD39$^+$CD9$^+$ IMs from normal untreated mouse lungs using FACS sorting, and then analyzed the cell death of CD39$^+$CD9$^+$ IMs in the presence or absence of recombinant IL-23 (rIL-23). rIL-23 treatment increased the late apoptosis (AnnexinV$^+$/PI$^+$) of CD39$^+$CD9$^+$ IMs (Fig. 3i, j). Moreover, IL-23 receptor neutralizing antibody (αIL-23r) treatment reversed the increased rIL-23-induced death of CD39$^+$CD9$^+$ IMs at the basal level (Fig. 3i, j). In contrast, CD39$^-$CD9$^-$ monocytes showed no significant responses to IL-23 or αIL-23r. These findings were further confirmed by FACS analysis with antibodies against AnnexinV and PI (Fig. 3k). These data suggest that the increased IL-23 in OVA + LPS/OVA reduces CD39$^+$CD9$^+$IMs by inducing cell death.

CD39 and CD9 are responsible for αIL-23p19-dependent suppression of Th17 cell activation and neutrophilic inflammation in NDA mice

To examine the functional roles of CD39 and CD9 on CD39$^+$CD9$^+$ IMs, we next treated POM1, a CD39 inhibitor, or a CD9 neutralizing antibody (αCD9) in OVA + LPS/OVA + αIL-23p19 where CD39$^+$CD9$^+$IM counts were restored. Intriguingly, the increased percentage of CD39$^+$CD9$^+$ IMs by αIL-23p19 was returned to the level in OVA + LPS/OVA by POM1 or αCD9 administration (Fig. 4a). Correspondingly, the decreased percentages of neutrophils in the lung and the decreased counts of total cells and neutrophils in BALF, as well as the decreased levels of Th17-related cytokines (IL-17 and IL-22) in BALF after αIL-23p19 administration was returned to the levels before αIL-23p19 administration (OVA + LPS/OVA) by POM1 or αCD9 administration (OVA + LPS/OVA + αIL-23p19 + POM1 or αCD9 in Fig. 4b–e). Immune cell infiltration (Fig. 4f, g) and P_{enh} values (Fig. 4h) also showed similar alteration patterns by POM1 and αCD9. Consistent with the above finding in Fig. 3g, h, POM1 or αCD9 administration had no effect on the percentage of IL-10-producing CD39$^+$CD9$^+$ IMs in lung and IL-10 level in BALF (Supplementary Fig. 8c, d). Of note, however, POM1 and αCD9-showed no effects in OVA + LPS/OVA because CD39$^+$CD9$^+$IM levels were already decreased in this condition. Moreover, to examine the synergistic effect of POM1 and αCD9, we treated POM1 and αCD9 (POM1 + αCD9) simultaneously. The extent to abolish the inhibitory effects of αIL-23p19 was found to be similar between the co-administration and individual administrations (Supplementary Fig. 9a–i), indicating no significant synergistic effect. In contrast, without αIL-23p19 administration, the percentage of CD39$^+$CD9$^+$ IMs was not significantly affected by POM1 or αCD9 (OVA + LPS/OVA + POM1 or αCD9 in Fig. 4a), neither were the percentage of neutrophils in the lung, the cytokine levels in BALF, immune cell infiltration, and P_{enh} values (Fig. 4b, e–h). Taken together, these data suggest that both CD39 and CD9 are required for the inhibitory effects of αIL-23p19.

CD39$^+$CD9$^+$ IMs suppress IL-23-mediated Th17 cell activation and neutrophilic inflammation by inhibiting NETosis

We next investigated how CD39$^+$CD9$^+$ IMs suppress IL-23-mediated neutrophilic inflammation in NDA mice. CD39 is reported to suppress the formation of neutrophil extracellular traps, called NETosis, in venous thrombosis mouse models[52], suggesting the association of CD39 with NETosis in the NDA model. To test this possibility, we first compared the extent of NETosis in the lungs by measuring citrullinated histone H3 (citH3)- and MPO-positive NET-stained areas in OVA + LPS/PBS, OVA + LPS/OVA, OVA + LPS/OVA + GSK484 (NETosis inhibitor; PAD4 inhibitor), and OVA + LPS/OVA + αIL-23p19. NETosis was increased in OVA + LPS/OVA, compared to in OVA + LPS/PBS, which was significantly attenuated by GSK484 or αIL-23p19 (Fig. 5a, b). Moreover, the attenuated NETosis in OVA + LPS/OVA + αIL-23p19 was increased back to the level in OVA + LPS/OVA by POM1 administration, which was re-attenuated by GSK484 administration (OVA + LPS/OVA + αIL-23p19 + POM1 + GSK484). Although CD9 has not been reported to be involved in NETosis in allergic airway inflammation, αCD9 administration led to similar results to POM1 administration (Fig. 5a, b). Moreover, co-administration of POM1 and αCD9 showed the same effect on NETosis with similar extents to the individual administrations (Supplementary Fig. 9j, k). Furthermore, the effects of POM1 or αCD9 on neutrophilic inflammation, Th17 cell activation, and P_{enh} values (Fig. 5c–i), as well as IL-23 level and CD39$^+$CD9$^+$ IM percentage (Fig. 5j, k), in OVA + LPS/OVA + αIL-23p19, were abolished by GSK484. We further confirmed similar results in the HDM models to those in the OVA models (Supplementary Fig. 10a–j). Taken together, these data indicate that CD39$^+$CD9$^+$ IMs suppress IL-23-mediated Th17 cell activation and neutrophilic inflammation by inhibiting NETosis in both OVA- and HDM-driven asthma models.

CD39$^+$CD9$^+$ IMs directly inhibit NETosis of neutrophils derived from NDA mice in CD39 and CD9-dependent manner

We next investigated whether CD39$^+$CD9$^+$ IMs directly inhibit NETosis or via other indirect mechanisms. To this end, we isolated Ly6G$^+$CD11b$^+$CD11c$^-$ neutrophils and CD39$^+$CD9$^+$ IMs from mouse lungs in OVA + LPS/OVA and OVA + LPS/OVA + αIL-23p19, respectively. We then analyzed the NETosis of the isolated neutrophils in the presence or absence of CD39$^+$CD9$^+$ IMs (Supplementary Fig. 11a). High levels of NETosis were observed in the absence of CD39$^+$CD9$^+$ IMs, which also indicates that neutrophils isolated from OVA + LPS/OVA are already

https://doi.org/10.1038/s41467-024-53038-2

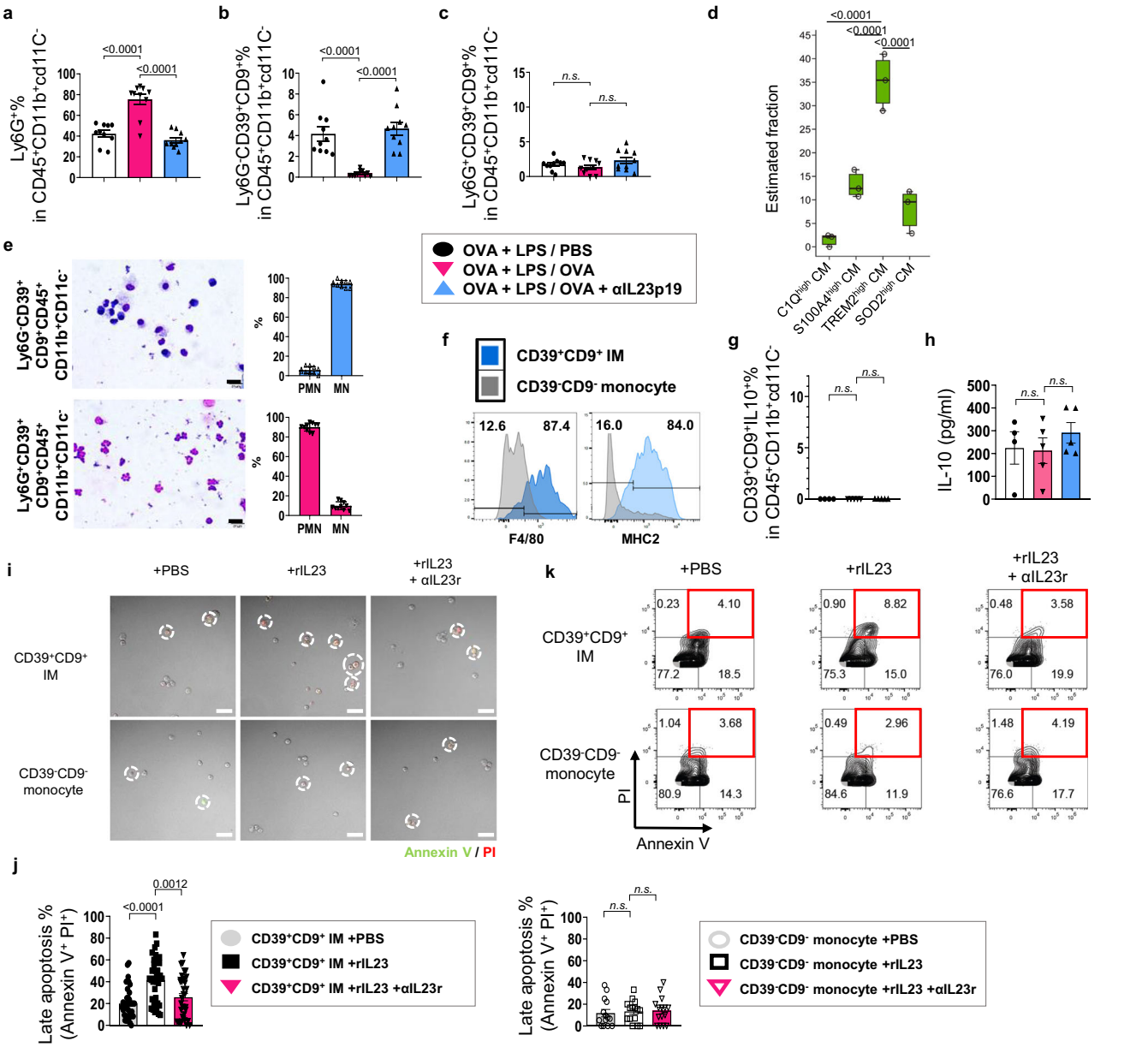

Fig. 3 | Myeloid cell subpopulations identified by single-cell analyses were CD39$^+$CD9$^+$ IMs. a Percentages of Ly6G$^+$ neutrophils, **b** Ly6G$^-$CD39$^+$CD9$^+$ IMs, and **c** Ly6G$^+$CD39$^+$CD9$^+$ neutrophils in CD45$^+$CD11b$^-$CD11c$^-$ cells of lung under the indicated conditions. (**a**–**c**, $n = 10$ per group). **d** Estimated fractions of CM subclusters in CD39$^+$CD9$^+$ IMs ($n = 3$ per group). In the box plots, the center line indicates the median value, the box limits indicate the upper and lower quartiles and the whiskers indicate the minimum and maximum. **e** Percentages of mononuclear (MN) and polymorphonuclear (PMN) cells in CD39$^+$CD9$^+$ IMs (blue bars) or Ly6G$^+$ neutrophils (red bars) measured by Wright–Giemsa staining (right) ($n = 10$ per group). Representative staining images are shown (left). **f** Histograms of F4/80 and MHCII expression levels of CD39$^+$CD9$^+$ IMs (blue) or CD39$^-$CD9$^-$ monocytes (gray). **g** Percentage of IL10$^+$CD39$^+$CD9$^+$ IMs in the lung. **h** Level of IL-10 in BALF (**g**, **h**; OVA + LPS/PBS ($n = 4$), OVA + LPS/OVA ($n = 5$), and OVA + LPS/OVA + αIL-23p19 ($n = 5$)). **i** Representative images of immunostaining for PI (red), Annexin V-FITC (green), and T-PMT (light). Scale bar = 20 μm. **j** Percentage of CD39$^+$CD9$^+$ IMs ($n = 36$ per group), or CD39$^-$CD9$^-$ monocytes ($n = 15$ per group) undergoing late apoptosis (Annexin V$^+$/PI$^+$) in field of view (FOV). **k** flow cytometry plot of Annexin V and PI. Data are shown as mean ± s.e.m. Significance was determined by using one-way ANOVA with Tukey's multiple comparison tests (**a**–**d**, **g**, **h**, **j**).

activated. However, NETosis was significantly decreased in the presence of CD39$^+$CD9$^+$ IMs (Fig. 6a, b). CD39$^+$CD9$^+$ IMs isolated from untreated control mice (PBS/PBS) also showed similar inhibition effects on NETosis to those from OVA + LPS/OVA + αIL-23p19 mice (Supplementary Fig. 11b–d). However, the inhibition of NETosis by CD39$^+$CD9$^+$ IMs was abolished by POM1 treatment, while it was not observed when CD39$^-$CD9$^-$ monocytes were used instead of CD39$^+$CD9$^+$ IMs (Fig. 6a, b). To examine whether CD39$^+$CD9$^+$ IM-mediated ectonucleotidase activity is responsible for suppressing NETosis ex vivo, we analyzed NETosis in the presence of CD39$^+$CD9$^+$ IMs after treatment with various concentrations of ATP. Suppression of NETosis by CD39$^+$CD9$^+$ IMs was reversed by 1 or 100 μM of ATP, but not by 0.01 or 0.1 μM of ATP (Fig. 6a, b). These data indicate that CD39 within CD39$^+$CD9$^+$ IMs directly inhibit NETosis through ATP hydrolysis. Moreover, we investigated whether CD9, a tetraspanin protein involved in cell adhesion, within CD39$^+$CD9$^+$ IMs can also directly suppress NETosis. To this end, we tested whether CD39$^+$CD9$^+$ IMs were attached to neutrophils 2 hr after adding CD39$^+$CD9$^+$ IMs to neutrophils. MHCII-positive CD39$^+$CD9$^+$ IMs (red) were physically attached to neutrophils (non-red), while neutrophils were scattered in the

https://doi.org/10.1038/s41467-024-53038-2

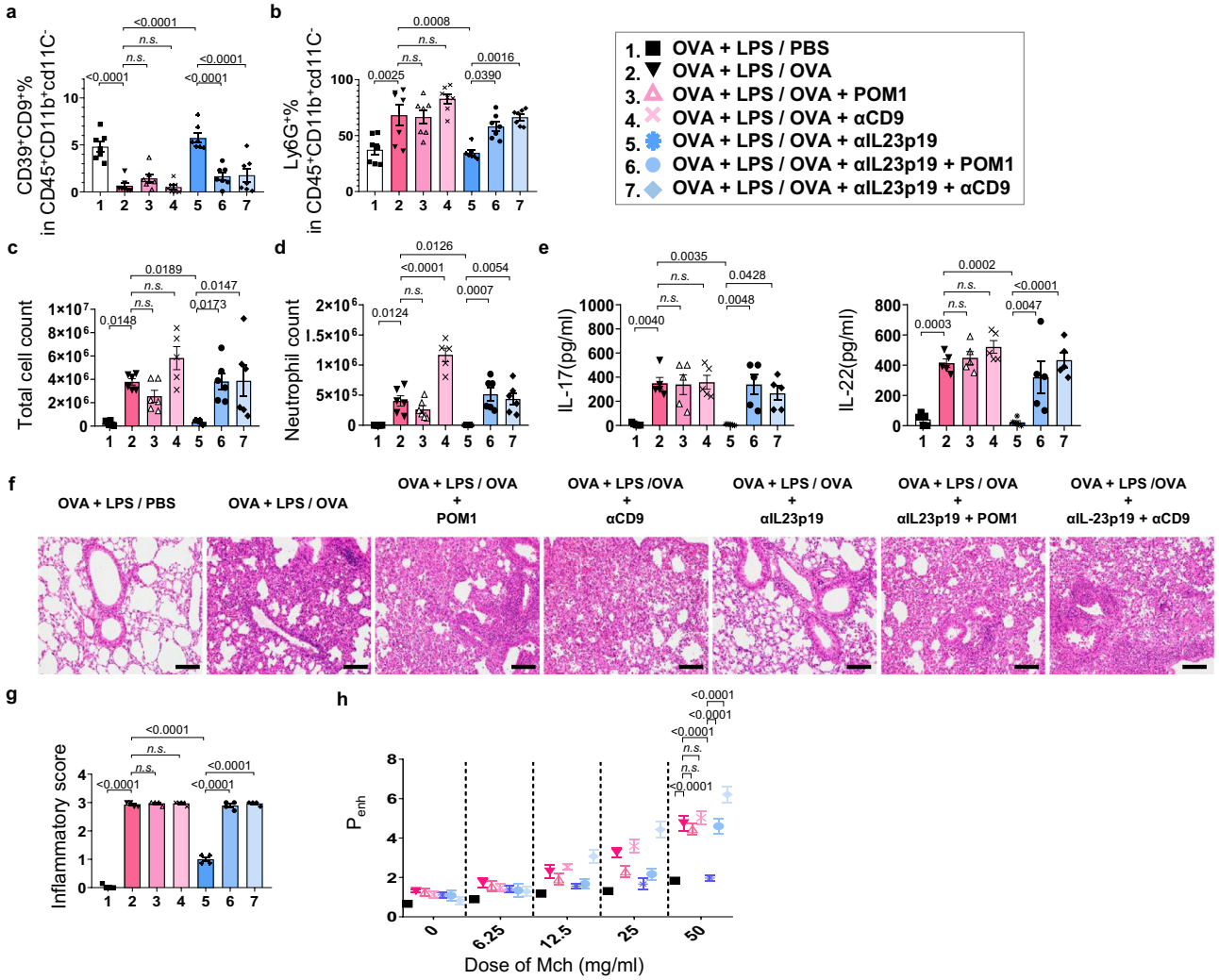

Fig. 4 | CD39 and CD9 are responsible for αIL-23p19-dependent suppression of Th17 cell activation and neutrophilic inflammation in NDA mice. a Percentages of $CD39^+CD9^+$ IMs and (**b**) $Ly6G^+$ neutrophils in $CD45^+CD11b^-CD11c^-$ cells of lung ($n = 7$ per group). **c** Total cell, (**d**) neutrophil counts in 7 groups: (i) OVA + LPS/PBS ($n = 6$), (ii) OVA + LPS/OVA ($n = 6$), (iii) OVA + LPS/OVA + POM1 ($n = 6$), (iv) OVA + LPS/OVA + αCD9 ($n = 5$), (v) OVA + LPS/OVA + αIL-23p19 ($n = 6$), (vi) OVA + LPS/OVA + αIL-23p19 + POM1 ($n = 6$), and (vii) OVA + LPS/OVA + αIL-23p19 + αCD9 ($n = 6$). **e** IL-17 and IL-22 levels in BALF ($n = 5$ per group). **f** Representative images of H&E staining and (**g**) inflammatory scores quantified from H&E staining ($n = 4$ per group). Scale bar = 100 μm. **h** P_{enh} values were measured using whole-body plethysmography ($n = 6$ per group). Data are shown as mean ± s.e.m. Significance was determined by one-way ANOVA with Tukey's post hoc correction (**a**–**e**, **g**) and two-way ANOVA with Sidak's post hoc correction (**h**).

absence of $CD39^+CD9^+$ IMs or in the presence of $CD39^-CD9^-$ monocytes (Fig. 6c, d). However, neutrophils held by $CD39^+CD9^+$ IMs were separated by αCD9 treatment (Fig. 6c, d). Moreover, the attachment of $CD39^+CD9^+$ IMs to neutrophils drastically decreased NETosis, while no attachment by $CD39^-CD9^-$ monocytes or the deceased attachment by αCD9 treatment led to the induction of NETosis (Fig. 6e, f). These data indicate that CD9 contributes to the attachment of $CD39^+CD9^+$ IMs to neutrophils. Although the attachment was not blocked by POM1 treatment or ATP addition (Fig. 6c, d), high amounts of ATP nearby neutrophils still induce NETosis (Fig. 6e, f). Taken together, our results indicate that both CD9 and CD39 on $CD39^+CD9^+$ IMs are required for the suppression of NETosis in NDA conditions: $CD39^+CD9^+$ IMs first attach to neutrophils in a CD9-dependent manner, and then remove ATP molecules near neutrophils in a CD39-dependent manner.

All our results can collectively provide a model (Supplementary Fig. 12) describing regulatory relationships among the five components; IL-23, Th17 cell activation, neutrophilic inflammation, NETosis, and $CD39^+CD9^+$ IMs. IL-23 induces Th17 cell activation that leads to neutrophil inflammation and NETosis (Pathways 1–3). We showed above that IL-23 inhibited $CD39^+CD9^+$ IMs (Pathway 4), which suppressed NETosis (Pathway 5). Interestingly, our results also revealed that $CD39^+CD9^+$ IMs also suppressed Th17 cell activation and neutrophilic inflammation. Our following results suggest that NETosis can increase IL-23 levels (Pathway 6), which was previously demonstrated by several studies[53–55]: (1) inhibition of NETosis in OVA + LPS/OVA by GSK484 decreased the IL-23 level in BALF (OVA + LPS/OVA + GSK484 in Fig. 5j); and (2) when the increased NETosis in OVA + LPS/OVA + αIL-23p19 + POM1 or αCD9 was re-attenuated by GSK484 (Fig. 5a, b), the IL-23 level was decreased. Accordingly, $CD39^+CD9^+$ IMs could suppress Th17 cell activation and neutrophilic inflammation by inhibiting Pathways 5 and 6. To further investigate regulatory links of Th17 cell activation to $CD39^+CD9^+$ IMs and NETosis, we treated αIL-17 in OVA + LPS/OVA and found that αIL-17 administration strongly reduced the increased NETosis and neutrophilic inflammation in OVA + LPS/OVA (Supplementary Fig. 13a–c; Pathways 2 and 3 in Supplementary Fig. 12), but increased $CD39^+CD9^+$ IMs (Supplementary Fig. 13d; Pathways 6 and 4 in Supplementary Fig. 12). This model demonstrates that $CD39^+CD9^+$ IMs serve as an important regulatory axis that inhibits NETosis as an

https://doi.org/10.1038/s41467-024-53038-2

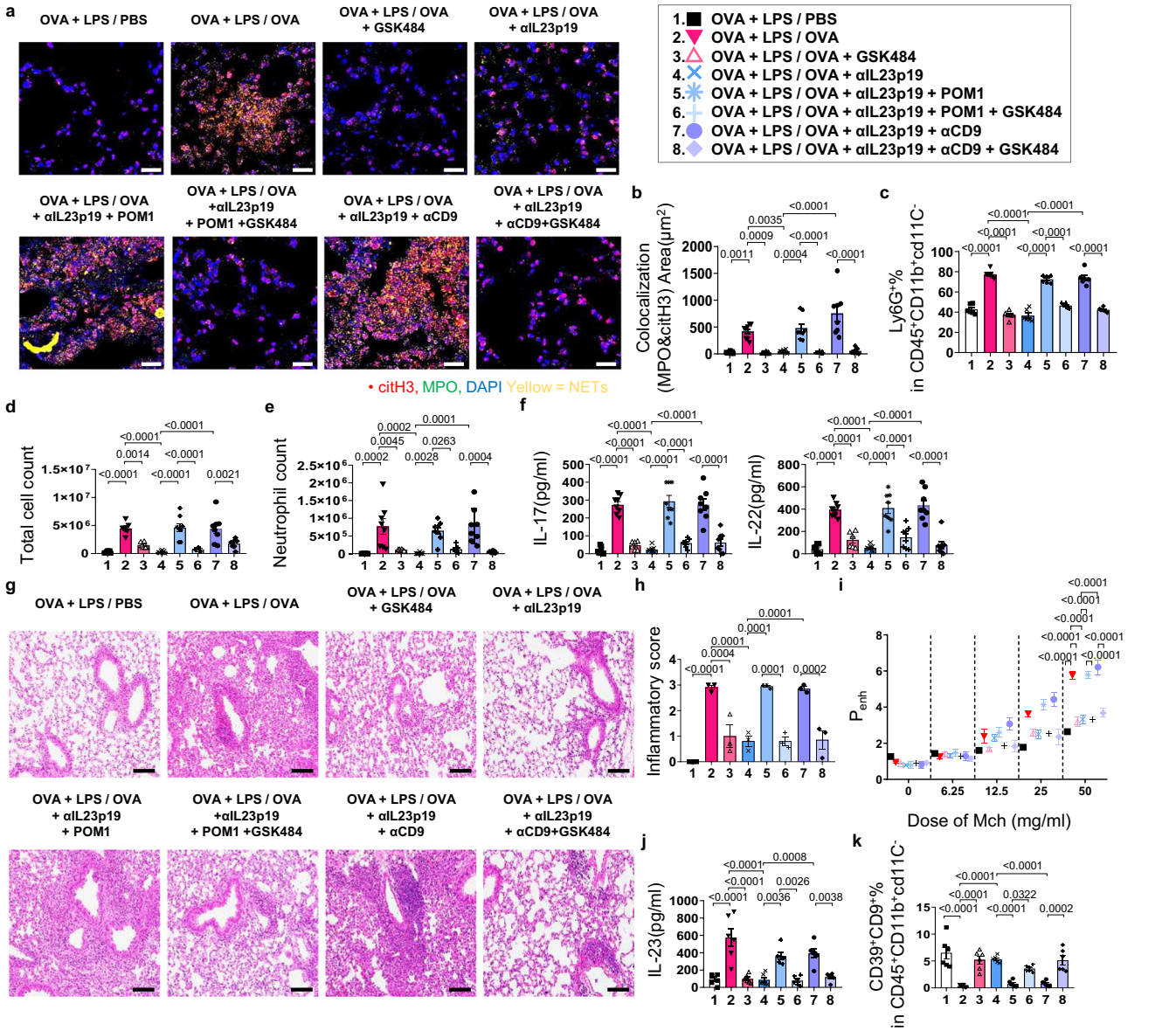

Fig. 5 | CD39⁺CD9⁺ IMs are critical for αIL-23p19-dependent suppression of neutrophilic inflammation via inhibition of NETosis. a Representative images of lung immunostaining for citrullinated histone H3 (citH3, red), MPO (green), and DAPI (blue). citH3⁺MPO⁺ NETs are shown in yellow. Scale bar = 20 μm. **b** Colocalization area (μm²) of citH3⁺MPO⁺ NETs in each FOV quantified using Zen software ($n = 8$ per group). **c** Ly6G⁺ neutrophil percentage in the lung ($n = 6$ per group). **d** total cell, (**e**) neutrophil counts in BALF and, (**f**) IL-17 and IL-22 levels in BALF (OVA + LPS/PBS ($n = 8$), OVA + LPS/OVA ($n = 8$), OVA + LPS/OVA + GSK484 ($n = 6$), OVA + LPS/OVA + αIL-23p19 ($n = 8$), OVA + LPS/OVA + αIL-23p19 + POM1 ($n = 8$), OVA + LPS/OVA + αIL-23p19 + POM1 + GSK484 ($n = 8$), OVA + LPS/OVA + αIL-23p19 + αCD9 ($n = 8$), and OVA + LPS/OVA + αIL-23p19 + αCD9 + GSK484 ($n = 8$)). **g** Representative images of H&E staining and (**h**) inflammatory scores quantified from H&E staining. Scale bar = 100 μm ($n = 3$ per group). **i** P_{enh} values measured using a whole body plethysmography (OVA + LPS/PBS ($n = 8$), OVA + LPS/OVA ($n = 8$), OVA + LPS/OVA + GSK484 ($n = 8$), OVA + LPS/OVA + αIL-23p19 ($n = 8$), OVA + LPS/OVA + αIL-23p19 + POM1 ($n = 8$), OVA + LPS/OVA + αIL-23p19 + POM1 + GSK484 ($n = 8$), OVA + LPS/OVA + αIL-23p19 + αCD9 ($n = 6$), and OVA + LPS/OVA + αIL-23p19 + αCD9 + GSK484 ($n = 4$)). **j** IL-23 level in BALF ($n = 6$ per group) and (**k**) percentages of CD39⁺CD9⁺ IMs in CD45⁺CD11b⁺CD11c⁻ cells in the lung ($n = 6$ per group). Data are shown as mean ± s.e.m. Significance was determined by one-way ANOVA with Tukey's post hoc correction (**b**–**f**, **h**, **j**, **k**) and two-way ANOVA with Sidak's post hoc correction (**i**).

endogenous brake to suppress the IL-23-mediated Th17 cell activation-neutrophilic inflammation axis.

Adoptive transfer of CD39⁺CD9⁺ IMs ameliorates Th17 cell activation and neutrophilic inflammation in NDA mouse lungs

We have shown the functional roles of CD39⁺CD9⁺ IMs through inhibition of CD9 and/or CD39. To further test whether CD39⁺CD9⁺ IMs themselves can ameliorate directly the pathology of neutrophilic asthma, we intravenously injected (1) PBS (non-cellular negative control), (2) CD39⁺CD9⁺ IMs isolated from OVA + LPS/OVA + αIL-23p19 mice, (3) CD39⁺CD9⁺ IMs isolated from PBS/PBS mice, and (4) Ly6G⁺CD39⁺CD9⁺CD11b⁺CD11c⁻ cells (CD39⁺CD9⁺ neutrophils as negative control; Supplementary Fig. 8b) into NDA mice (Fig. 7a). Due to residual amounts of CD39⁺CD9⁺ IMs in OVA + LPS/OVA (Fig. 3b), we could not acquire a sufficient number of CD39⁺CD9⁺ IMs even after pulling CD39⁺CD9⁺ IMs isolated from more than 10 mice. Our findings above (Fig. 2d, e and Supplementary Fig. 11c, d) suggested the shared functional characteristics of CD39⁺CD9⁺ IMs from PBS/PBS, OVA + LPS/OVA, or OVA + LPS/OVA + αIL-23p19. We thus isolated CD39⁺CD9⁺ IMs as donor cells from CD45.1⁺ mice in PBS/PBS or OVA + LPS/OVA + αIL-23p19 and injected 2.5 to 3.5 × 10⁴ CD39⁺CD9⁺ IMs four times on days 14, 15, 21, and 22, based on which the total number of transferred donor

https://doi.org/10.1038/s41467-024-53038-2

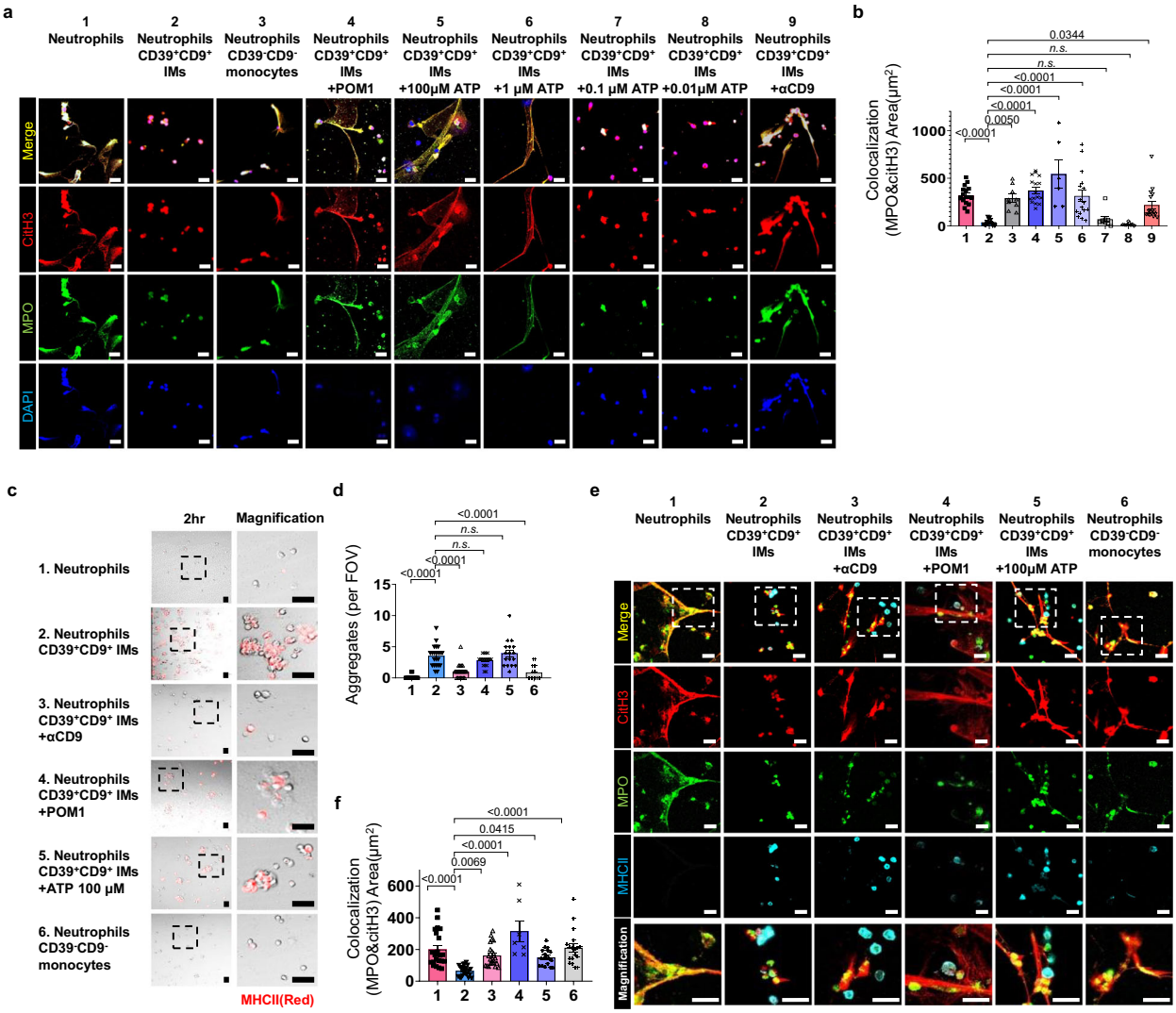

Fig. 6 | CD39⁺CD9⁺ IMs directly inhibit NETosis of neutrophils derived from NDA mice in CD39 and CD9-dependent manner. a Representative confocal microscopy images of immunostaining for citH3 (red), MPO (green), and DAPI (blue) in co-cultured slides. Merged citH3⁺MPO⁺ NETs are shown in yellow. Ly6G⁺ neutrophils were co-cultured with CD39⁺CD9⁺ IMs or CD39⁻CD9⁻ monocytes on chamber slides. **b** Colocalization area (μm²) of citH3⁺MPO⁺ NETs in each FOV quantified using Zen software (Neutrophils ($n = 16$), Neutrophils+CD39⁺CD9⁺ IMs ($n = 16$), Neutrophils+CD39⁻CD9⁻ monocytes ($n = 9$), Neutrophils+CD39⁺CD9⁺ IMs + POM1 ($n = 16$), Neutrophils + CD39⁺CD9⁺ IMs + 100 μM ATP ($n = 6$), Neutrophils+CD39⁺CD9⁺ IMs + 1 μM ATP ($n = 16$), Neutrophils+CD39⁺CD9⁺ IMs + 0.1 μM ATP ($n = 9$), Neutrophils+CD39⁺CD9⁺ IMs + 0.01 μM ATP ($n = 9$), and Neutrophils + CD39⁺CD9⁺ IMs + αCD9 ($n = 16$). **c** Representative photomultiplier tube (PMT) images showing immunostaining for MHCII (red) taken after 2 hr in the co-culture system. **d** Number of cell aggregates per FOV. Aggregates were defined as cells that adhered to at least five other cells (Netrophils ($n = 22$), Neutrophils + CD39⁺CD9⁺ IMs ($n = 22$), Neutrophils + CD39⁺CD9⁺ IMs + αCD9 ($n = 22$), Neutrophils+CD39⁺CD9⁺ IMs + POM1 ($n = 17$), Neutrophils+CD39⁺CD9⁺ IMs + 100 μM ATP ($n = 17$), and Neutrophils + CD39⁻CD9⁻ monocytes ($n = 17$)). **e** Representative confocal microscopy images of immunostaining for citH3 (red), MPO (green), and MHCII (blue) in co-cultured slides. **f** Colocalization area (μm²) of citH3⁺MPO⁺ NETs in each FOV. Scale bar = 20 μm. (Netrophils ($n = 22$), Neutrophils + CD39⁺CD9⁺ IMs ($n = 22$), Neutrophils + CD39⁺CD9⁺ IMs + αCD9 ($n = 22$), Neutrophils + CD39⁺CD9⁺ IMs + POM1 ($n = 7$), Neutrophils+CD39⁺CD9⁺ IMs + 100 μM ATP ($n = 18$), and Neutrophils + CD39⁻CD9⁻ monocytes ($n = 18$)). Data are shown as mean ± s.e.m. Significance was determined by one-way ANOVA with Tukey's post hoc correction (**b**, **d**, **f**).

cells was estimated to be approximately 10^5 cells and more. The 10^3 donor cells were found to be present in the lung of the recipient CD45.2⁺ mice under OVA + LPS/OVA for 24 days (Supplementary Fig. 14). The transfer of CD39⁺CD9⁺ IMs, but not CD39⁺CD9⁺ neutrophils, significantly reduced total cell and neutrophil counts in BALF, neutrophil percentage in the lung, RORγt⁺ Th17 cell count, and the levels of Th17-related cytokines (IL-17 and IL-22) (Fig. 7b–e), as well as IL-23 level (Fig. 7f) and immune cell infiltration (Fig. 7g, h). Transferred CD39⁺CD9⁺ IMs also enhanced respiratory function, such as P_{enh} values (Fig. 7i), but reduced citH3- and MPO-positive NET-stained areas in the lungs, suggesting that transferred CD39⁺CD9⁺ IMs suppressed NETosis (Fig. 7j, k). The transfer of CD39⁺CD9⁺ IMs isolated from untreated control mice (PBS/PBS) also showed similar effects to those from OVA + LPS/OVA + αIL-23p19 mice (Fig. 7b–k). Taken together, these results suggest that the transfer of CD39⁺CD9⁺ IMs can alleviate the pathology of neutrophilic asthma.

Finally, to examine the clinical relevance of CD39⁺CD9⁺ IMs, we assessed their proportions in lung tissues of patients with mild/moderate and severe asthma. To this end, we obtained bulk RNA expression profiles of lung tissues collected from asthma patients via bronchial epithelial brushing [SARP (GSE63142)] from the Gene Expression Omnibus (GEO) database. Among 126 patients with the

https://doi.org/10.1038/s41467-024-53038-2

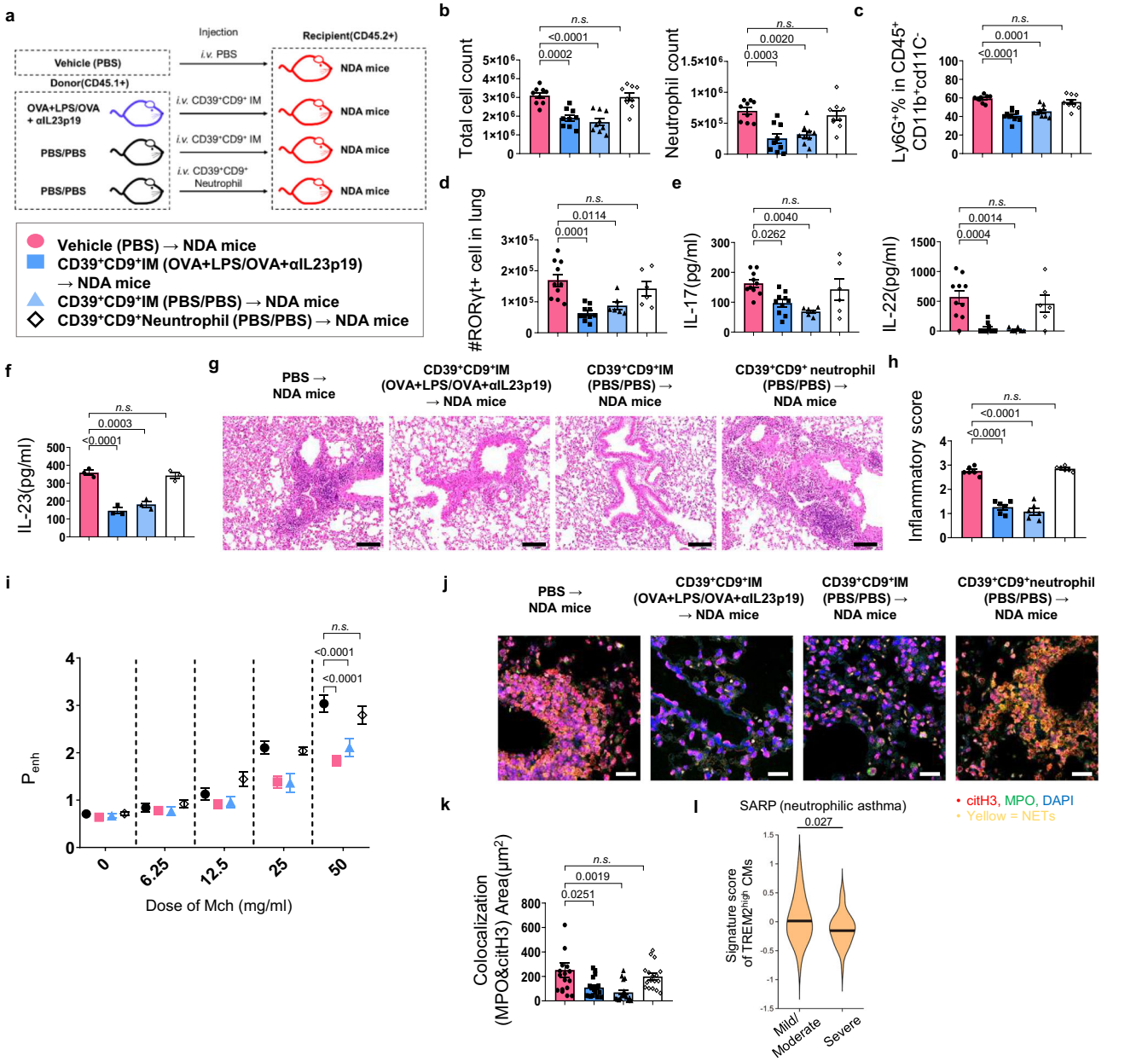

Fig. 7 | CD39⁺CD9⁺ IMs from PBS/PBS or OVA + LPS/OVA + αIL-23p19 suppress Th17-mediated neutrophilic inflammation in NDA mice. a Schematic diagram of the adoptive transfer protocol. CD39⁺CD9⁺ IMs were sorted from OVA + LPS/OVA + αIL-23p19 or PBS/PBS, while Ly6G⁺CD39⁺CD9⁺ neutrophils were sorted from PBS/PBS on day 24. These isolated cells were intravenously transferred on every challenge to the NDA mouse model. The inflammatory response was assessed at 48 hr after the last challenge. **b** Total cell and neutrophil counts in BALF. **c** Percentages of Ly6G⁺ neutrophils (**b**, **c**; $n = 9$ per group). **d** RORγt⁺ Th cells in CD4⁺ T cells in the lung. **e** Levels of IL-17 and IL-22 in BALF (**d**, **e**; Vehicle (PBS) → NDA mice ($n = 10$), CD39⁺CD9⁺ IM (OVA + LPS/OVA+αIL23p19)→NDA mice ($n = 10$), CD39⁺CD9⁺ IM (PBS/PBS) → NDA mice ($n = 6$), and Ly6G⁺CD39⁺CD9⁺ neutrophil IM (PBS/PBS) → NDA mice ($n = 6$)). **f** IL-23 in BALF ($n = 3$ per group). **g** Representative images of H&E staining and (**h**) inflammatory scores quantified from H&E staining ($n = 6$ per group). Scale bar = 100 μm. **i** P_{enh} values were measured using a whole body plethysmography. (Vehicle (PBS) → NDA mice ($n = 10$), CD39⁺CD9⁺ IM (OVA + LPS/OVA +αIL23p19)→NDA mice ($n = 10$), CD39⁺CD9⁺ IM (PBS/PBS) → NDA mice ($n = 6$), and Ly6G⁺CD39⁺CD9⁺ neutrophil IM (PBS/PBS) → NDA mice ($n = 6$)). **j** Representative images of lung immunostaining for citH3 (red), MPO (green), and DAPI (blue). The citH3⁺MPO⁺ NETs are shown in yellow. **k** Colocalization area (μm²) of citH3⁺MPO⁺ NETs ($n = 17$ per group). Scale bar = 20 μm. **l** Violin plots showing distributions of the signature scores of TREM2^{high} CM in patients with mild/moderate ($n = 30$) and severe asthma ($n = 33$) in the SARP cohort. Center line, median value. Data are shown as mean ± s.e.m. Significance was determined by one-way ANOVA with Tukey's post hoc correction (**b**–**f**, **h**, **k**), two-way ANOVA with Sidak's post hoc correction (**i**), and one-tailed Student's *t* test (**l**).

blood neutrophil percentage information in the SARP cohort, we next selected the patients that had potentially neutrophilic asthma as the ones having the mean neutrophil percentage of 59.5%, which included 30 mild/moderate and 33 severe patients. To predict the amount of TREM2^{high} CMs (CD39⁺CD9⁺ IMs) in each selected sample, we identified marker genes upregulated in TREM2^{high} CMs compared to all the other CD45⁺ immune cells from scRNA-seq data (Supplementary Fig. 15a) and then calculated signature scores for CD39⁺CD9⁺ IMs using the bulk RNA data of the sample based on the expression levels of the marker genes (Supplementary Fig. 15b). Severe asthmatic patients showed a significantly ($P < 0.05$) lower signature scores of CD39⁺CD9⁺ IMs than mild/moderate asthmatic patients (Fig. 7l), suggesting a possibility that decreased CD39⁺CD9⁺ IMs may contribute to severity of neutrophilic asthma.

Discussion

In neutrophilic asthma, the IL-23-Th17 axis plays a critical role in the recruitment and activation of neutrophils[56]. Our results identified a potent endogenous brake that could inhibit Th17 cell activation and was also suppressed itself by IL-23 (IL-23⊣CD39$^+$CD9$^+$ IMs⊣Th17 activation). What is then the value of having this brake? Together with the IL-23-Th17 pathway, the CD39$^+$CD9$^+$ IM-mediated inhibition pathway forms a coherent type 4 feed-forward loop (c4FFL)[57] (Supplementary Fig. 16a). According to the characteristics of FFLs[57], c4FFL causes a delay in Th17 cell activation until CD39$^+$CD9$^+$ IMs are completely suppressed, which makes Th17 cell activation robust against non-systematic variations of IL-23 in the microenvironment under normal conditions. In NDA conditions, the increased IL-23 suppresses CD39$^+$CD9$^+$ IMs, which deactivates the endogenous brake to activate the feedback loop between NETosis and IL-23 (Supplementary Fig. 16b, c), thereby aggravating neutrophilic inflammation.

Previously, Risankizumab, an IL-23 blockade, was reported to be ineffective in clinical trials for severe asthma[58]. While IL-23 blockades deactivate all pathways related to Th17 activation and neutrophil inflammation, CD39$^+$CD9$^+$ IMs can be used as an alternative to directly target NETosis, which in turn reduces IL-23 level, Th17 cell activation, and neutrophilic inflammation (Supplementary Fig. 16d). It would be interesting to study 1) whether risankizumab could affect CD39$^+$CD9$^+$ IMs in the lungs of severe asthmatic patients as effectively as demonstrated by adoptive transfer experiments and 2) whether the amount of CD39$^+$CD9$^+$ IMs differs between the patients in whom risankizumab was effective and ineffective. Although these issues need to be addressed by further experiments, combinatorial therapeutic strategies using CD39$^+$CD9$^+$ IMs and IL-23 blockade can be proposed to improve therapeutic control of severe neutrophilic asthma. Of note, CD39$^+$CD9$^+$ IMs showed higher expression levels of SPP1, GPNMB, FABP5, and CD63 than the other CM subpopulations. Previously, CD9$^+$TREM2$^+$ scar-associated macrophages (SAMs) were shown to have high expression levels of these marker genes and promote fibrosis[59], suggesting potential associations between CD39$^+$CD9$^+$ IMs and CD9$^+$TREM2$^+$ SAMs. However, fibrosis was not substantial in our NDA conditions and was not affected by αIL-23p19, indicating that CD39$^+$CD9$^+$ IMs are unlikely to have functional associations with CD9$^+$TREM2$^+$ SAMs.

There were several unexpected observations or results whose interpretation is not straightforward. First, IFNγ production was markedly increased in OVA + LPS/OVA compared to the other treatment conditions, while T-bet$^+$ Th cell count in OVA + LPS/OVA was not. This discrepancy between T-bet$^+$ Th cell count and IFNγ level suggests other sources of IFNγ than T-bet$^+$ Th cells. Previously, IFNγ was reported to be secreted from NK cells as well[60]. However, our scRNA-seq data showed that the NK cell proportion was decreased in OVA + LPS/OVA, compared to in OVA + LPS/PBS, and then restored partly in OVA + LPS/OVA + αIL-23p19 (Supplementary Fig. 6c), indicating that NK cells are not likely responsible for the discrepancy. Many potential sources of IFNγ during airway inflammation have been reported, including activated T-bet$^+$ Th, CD8$^+$ T, and NK cells, as well as γδT cells, macrophages, DCs, NKT cells, and B cell[61], suggesting that some of these cells might be responsible for the discrepancy. Second, αCD9 administration unexpectedly led to a significant increase in neutrophil count without αIL-23p19 administration (OVA + LPS/OVA + αCD9) compared to the level in OVA + LPS/OVA (Fig. 4d), while POM1 administration showed no significant change of the count (OVA + LPS/OVA + POM1). In contrast, with αIL-23p19 administration, both αCD9 and POM1 administrations (OVA + LPS/OVA + αIL-23p19 + POM1 or αCD9) increased the neutrophil count similarly up to the level in OVA + LPS/OVA. These data suggest a potential difference in the effects of αCD9 and POM1 on neutrophil count between αIL-23p19-treated and untreated conditions. Despite the difference in neutrophil count, however, CD39$^+$CD9$^+$ IM count and IL-23, IL-17, and IL-22 levels were not significantly different from their levels in OVA + LPS/OVA after αCD9 and POM1 administrations, neither were they even in αIL-23p19-treated conditions, suggesting that the αCD9-mediated increase in neutrophil count is independent of CD39$^+$CD9$^+$ IMs, IL-23, and Th17 cell activation. Combing these implications, we presume that in OVA + LPS/OVA with decreased CD39$^+$CD9$^+$ IMs, the cells targeted by αCD9 are some unknown cells that express only CD9 but not CD39, and are capable of suppressing neutrophil infiltration in an IL-23-Th17 axis independent manner. In contrast, in OVA + LPS/OVA + αIL-23p19 with substantial CD39$^+$CD9$^+$ IM counts, CD39$^+$CD9$^+$ IMs appear to be a major target cell type of αCD9 and POM1. The differential proportions of cells targeted by αCD9 and POM1 can thus account for the discrepancy in their effects on neutrophil count. Third, co-administration of POM1 and αCD9 abolished the effect of αIL-23p19 on neutrophil count, but the abolishing extent was similar to that observed after the individual administrations (POM1 or αCD9 in Supplementary Fig. 9), indicating no synergistic effect and that both of CD9 and CD39 are thus required for CD39$^+$CD9$^+$ IMs to inhibit NETosis. Our ex vivo experiments suggest that CD9 attaches CD39$^+$CD9$^+$ IMs to neutrophils, and CD39 then hydrolyzes extracellular ATPs near the neutrophils attached to CD39$^+$CD9$^+$ IMs to inhibit NETosis, supporting the requirement of both CD9 and CD39 for NETosis suppression. Finally, CD39$^+$CD9$^+$ IM count in OVA + LPS/OVA was increased by GSK484 to the level in OVA + LPS/OVA + αIL-23p19, while IL-17 and IL-22 levels and neutrophil count were decreased to their levels in OVA + LPS/OVA + αIL-23p19, suggesting therapeutic effects of GSK484 comparable to αIL-23p19. Our model (Supplementary Figs. 12, 16b) provides a possible explanation for this observation that NETosis increases IL-23 level through the aforementioned positive feedback regulation, and GSK484 administration would thereby decrease the NETosis-mediated increase of IL-23 level, which in turn reduces IL-17 and IL-22 levels and neutrophil count.

With pre-challenge administration of αIL-23p19 (Fig. 1a), it might not be clear whether the effect of αIL-23p19 would be preventive or therapeutic. We showed that the inflammation developed during the sensitization returned to the basal level before the challenge. Interestingly, despite the restoration of IL-17 level to the basal level, RORγt$^+$ Th cell count was increased with OVA + LPS sensitization compared to that with PBS sensitization (Supplementary Fig. 3c, d), which may indicate a potentiation of Th17 response achieved by the sensitization. This potentiation can be considered an important aspect of our NDA model because it can account for the potent Th17-mediated neutrophilic inflammation observed during the OVA + LPS/OVA challenge in our NDA model. Moreover, the post-challenge administration of αIL-23p19 further showed the comparable suppression of neutrophilic inflammation to the pre-challenge administration. Given the restoration of the inflammation before the challenge, these data support that αIL-23p19 may have the potential therapeutic effect on neutrophilic inflammation in our NDA model. Of note, our 12 hr post-challenge model is based on a previous finding that neutrophil infiltration reaches a peak between 12 and 24 hr upon inflammatory stimulation[62].

It has been reported that sex hormones can affect IL-23 signaling and IL-17 production in severe asthma[63]. Specifically, females exhibited more severe symptoms than males due to alterations in Let-7f microRNA. Changes in sex hormones during the menstrual cycle and menopause could impact the severe asthma phenotype. We thus chose to use male mice in this study to minimize potential variations associated with sex hormones. However, further studies are needed to investigate our main findings in females. In addition, we evaluated whether the association of CD39$^+$CD9$^+$ IMs with the severity of neutrophilic asthma might vary with sex. To this end, we further divided mild/moderate and severe neutrophilic asthma groups in Fig. 7l by sex and performed the same signature score analysis for the resulting subgroups. Severe neutrophilic asthmatic patients were found to show lower signature scores of CD39$^+$CD9$^+$ IMs in both male and female

patients than mild/moderate patients, consistent with the finding in Fig. 7l. However, these patterns in male and female patients should be verified in a larger clinical cohort.

We showed that TNF and IL-6 levels were significantly elevated in OVA + LPS/OVA compared to in OVA + LPS/PBS control, and αIL-23p19 administration markedly reduced their levels in the same way it reduced the levels of Th17 cell activation and neutrophilic inflammation. Moreover, it was previously reported that anti-IL-6 treatment significantly reduced Th17 cell counts using HDM-derived severe asthmatic mouse models[42]. In addition, FB704A, an anti-IL-6 antibody, is currently under clinical trials as a therapeutic agent for severe neutrophilic asthma. Accordingly, our results and these previous findings collectively suggest the potential roles of TNF and IL-6, particularly IL-6, in Th17-mediated neutrophilic inflammation under severe asthmatic conditions. On the other hand, we showed that another cytokine, IL-22, showed similar expression patterns to IL-17 and neutrophil counts across the conditions (Fig. 5f). We presumed that IL-22 was secreted mainly from Th17 cells based on a previous report that IL-17A and IL-22 are simultaneously increased in $CD4^+$ T cells from the HDM-induced mouse asthma model[64]. However, IL-22 has also been shown to be a negative regulator of eosinophil inflammation and Th2 allergic responses[65]. Taken together, in our NDA models, our results and the previous findings suggest that IL-17 promotes neutrophilic inflammation while IL-22 may suppress eosinophil inflammation and Th2 responses, systematically leading to neutrophilic inflammation. The functional roles of these cytokines should be further investigated through detailed experiments.

Several reviews have summarized the limitations of mouse models in recapitulating clinical scenarios of NDA[66,67]. For example, considering that the inflammation was almost restored before the challenge in our NDA model, whether our findings would still be valid for a long time period after the last challenge remains uncertain. When we examined neutrophilic phenotypes at 2 weeks after the last challenge in our NDA models, the phenotypes were almost resolved. Given the above limitations of OVA and HDM models, however, a number of studies have also demonstrated the utility of these models for the purpose of investigating molecular mechanisms of NDA phenotypes, including steroid resistance, neutrophil invasion, and Th17 expansion[43,68]. The findings from our NDA models might be thus valid only during a short time period after the last challenge. It is then difficult to understand how the decreased $CD39^+CD9^+$IM can correlate with the severity of neutrophilic asthma in patients. One possible explanation might be that the exposures to allergens constantly occur locally in a heterogeneous manner across the lung with the mixed short and long-term phenotypes of neutrophilic asthma from one location to the other, which might contribute to collectively the increase of neutrophils in the blood and the decrease of $CD39^+CD9^+$IMs in the lung.

In summary, we demonstrated that the $CD39^+CD9^+$ IM axis identified from our OVA-driven model is present in an allergen extract-derived model HDM, and its functional roles in αIL-23p19-dependent suppression of neutrophilic inflammation are also valid in the HDM model. In addition, the signature scores estimated from bulk gene expression profiles of lung tissues in asthmatic patients suggested a potential association (i.e., inverse correlation) of $CD39^+CD9^+$ IM with asthma severity. However, the $CD39^+CD9^+$ IM axis and its functional role further needed to be confirmed in patients with severe neutrophil-associated asthma and to be comparatively evaluated in a large cohort, including patients with mild, moderate, and severe asthma. Moreover, after confirming their validity in severe asthma patients, how $CD39^+CD9^+$ IMs can be acquired for clinical use in practice is not straightforward. Adoptive transfer experiments demonstrated that $CD39^+CD9^+$ IMs isolated from PBS/PBS and OVA + LPS/OVA + αIL-23p19 conditions showed comparable therapeutic effects, suggesting a possible strategy for the acquisition of $CD39^+CD9^+$ IMs in normal conditions, which should be further investigated in a large cohort of asthma patients.

Methods

Study approval

All experiments were performed in accordance with the Association for Assessment and Accreditation of Laboratory Animal Care International (AAALAC International, facility no. 001071) guidelines and approved by the Institutional Animal Care and Use Committee (IACUC) at Yonsei University College of Medicine (protocol no. 2020-0261).

Mice

All mice used in this study were housed under specific pathogen-free (SPF) conditions and used at 6–8 weeks of age. Male C57BL/6 mice were purchased from Orient Bio (Gyeonggi, Korea) for the experiments. The mice were housed in SPF animal facilities, maintained under a 12-h light-dark cycle at 20 ± 2 °C, with 50 ± 5% humidity, ventilation of 10–15 air changes per hour, light intensity of 150–300 lux, and noise levels below 60 dB.

Generation of the NDA mouse models

In the OVA-driven NDA mouse model, mice were anesthetized with a Zoletil-Rompun mixture and then sensitized through intranasal instillation of OVA (75 μg, Grade V; Sigma-Aldrich, St. Louis, MO, USA) and LPS (10 μg) on days 0, 1, 2, and 7. On 7 days after the fourth sensitization, mice were anesthetized, challenged through intranasal instillation of OVA (100 μg) only on days 14, 15, 21, and 22, and then sacrificed on day 24. When quantified using a ToxinSensor chromogenic LAL Endotoxin assay kit (L00350, Genescript, USA), the OVA (100 μg) used was found to contain 5.77 EU LPS. In the HDM-driven NDA mouse model, mice were anesthetized with Zoletil-Rompun mixture and then sensitized through intranasal instillation of house dust mite extracts (HDM, 25 μg; XPB82D3A25, Greer Laboratories) and LPS (10 μg) on days 0, 1, and 2. On 7 days after the fourth sensitization, mice were anesthetized, challenged through intranasal instillation of HDM (6.25 μg) on days 14, 15, 18, and 19, and sacrificed on day 21. Installed HDM (25 μg) contained 20 EU LPS by Limulus amebocyte assay (Greer Laboratories).

Neutralizing antibody, dexamethasone, and inhibitor administration

Mice were pre-treated intraperitoneally (*i.p.*) with anti-IL-23p19 antibody (400 μg per mouse; BE0313, G23-8, BioxCell, West Lebanon, NH, USA) or dexamethasone (1 mg/kg per mouse; Sigma-Aldrich) 1 hr before the challenge, but not during the sensitization period. Control mice were treated with rat IgG2a isotype control antibody (400 μg per mouse; BE0089, 2A3, BioxCell). All inhibitors were pretreated *i.p.* 1 hr before the challenge: POM1 (20 mg/kg; Tocris Bioscience, Bristol, UK), anti-CD9 antibody (5 mg/kg; 553758, KMC8, BD Pharmingen, San Diego, CA, USA), anti-IL-17/IL-17A antibody (250 μg/kg; 50104, R&D Systems, Minneapolis, MN, USA), and GSK484 (PAD4 inhibitor; 4 mg/kg; Cayman Chemical, Michigan, USA).

Measurement of methacholine AHR levels

At 24 hr after the last OVA challenge (on day 23), responses to inhaled methacholine (Sigma-Aldrich) were measured in unrestrained mice using whole-body plethysmography (WBP; Buxco, Wilmington, NC, USA). Mice were nebulized for 3 min with PBS, followed by the administration of increasing concentrations of methacholine (6.25, 12.5, 25, and 50 mg/ml). Lung function was recorded for 2 min and calculated as enhanced pause (P_{enh}), which is a dimensionless unit that correlates with pulmonary resistance. Calculations were performed using FinePoint software (Buxco)[69]. Moreover, to measure AHR in an invasive manner, mice were anesthetized and operated via tracheostomy. The mice were connected using a metal cannula to FlexiVent

(Scirecq) and mechanically ventilated. To determine respiratory system resistance (R_{rs}), methacholine at multiple concentrations (0, 6.25, 12.5, 25, and 50 mg/ml) was nebulized. Snapshot150 and Quick Prime-3 perturbation were then recorded. Each value was repeated until acceptable measurements (coefficient of determination > 0.95) were recorded. The mean value of R_{rs} was then calculated[70].

Sample collection from blood, BALF, and lung tissue

Mice were sacrificed by an overdose of a Zoletil-Rompun mixture. Following the previously reported protocol[71], BALF was first acquired using 1 ml of cold PBS through the murine trachea. The aspiration was repeated twice until no further fluid was collected. BALF was centrifuged (1600 × *g*, 5 min), and the separated BALF supernatant was used to measure cytokine levels. The BALF pellets were used for cell counting and flow cytometry analysis. Next, we perfused 10 ml of PBS into the lungs through the right ventricle and extracted and fixed the left lobe of the lung for H&E, PAS, and immunofluorescence staining. The right lobes of the lung were extracted and chopped into small pieces. The lung tissues were homogenized using a collagenase dissociation solution [25 mg collagenase type II and 1 µl DNase in 5 ml Hank's balanced salt solution (HBSS) per mouse] for 1 hr at 37 °C. After dissociation, the samples were filtered through a 70 µm strainer twice and then centrifuged at 1600 × *g* for 5 min. The pellet was stained and analyzed using flow cytometry.

Flow cytometry

Single cells were lysed with red blood cell (RBC) lysis buffer for 3 min on ice and then centrifuged at 1600 × *g* for 5 min. After the supernatant was removed, the pellet was stained with an antibody (1:100) for 20 min on ice and then washed twice. The washed pellet was resuspended in PBS containing 2% fetal bovine serum (FBS) and filtered through a 40 µm strainer. The samples were then analyzed using flow cytometry. The cells obtained from BALF and lung samples were counted and stained with 4′,6-diamidino-2-phenylindole (DAPI), eFluor 450 anti-mouse Ly6G (48-9668-82, 1A8, eBioscience, San Diego, CA, USA), Percp/Cyanine 5.5-anti-mouse CD11c (117328, N418, Biolegend, San Diego, CA, USA), PE-anti-mouse CD170 (SiglecF) (155506, S17007L, Biolegend), FITC rat-anti mouse CD11b (553310, M1/70, BD Bioscience, San Jose, CA, USA), PE-Cy7 rat-anti mouse CD45 (552848, 30-F11, BD), AF700-rat anti-CD9 (NBP1-44876, EM-04, NOVUSBIO, Centennial, CO, USA), and PE/Dazzle 594 anti-mouse CD39 (143812, Duha59, Biolegend).

To examine the T cell population, the lung single-cell samples were stained with LIVE/DEAD Fixable Aqua Dead Cell Stain Kit (L34957, ThermoFisher), Percp/Cyanine 5.5-anti-mouse/human CD11b (M1/70, Biolegend), Percp/Cyanine 5.5-anti-CD14 (45-0141-82, Sa2-8, eBioscience), Percp/Cyanine 5.5-anti-CD19 (115533, 6D5, Biolegend), Percp/Cyanine 5.5-anti-B220 (45-0452-82, RA3-6B2, eBioscience), Percp/Cyanine 5.5-anti-I-A/I-E (107625, M5/114.15.2, Biolegend), Brilliant Violet 605-anti-mouse TCRβ chain (109241, H57-597, Biolegend), BV421 anti-mouse RORγt (562894, Q31-378, BD), Alexa Fluor 488-anti-FOXP3 (53-5773-82, FJK-16s, eBioscience), PE-CF594-anti-T-bet (562467, O4-46, BD), APC-eFluor-780 CD44 (47-0441-82, IM7, eBioscience), Brilliant Violet-711 anti-mouse CD4 (100557, RM4-5, Biolgend), and PE-anti-GATA3 (12-9966-42, TWAJ, eBioscience). For intracellular staining, the cells were processed using the FOXP3 transcription factor staining buffer set (00-5523-00, eBioscience) according to the manufacturer's protocol. Following a previously reported protocol used in asthmatic conditions[72], the stained cells were analyzed by sorting Th17 [liveDump$^-$(CD11b$^-$CD14$^-$CD19$^-$B220$^-$I-A/I-E$^-$)FOXP3$^-$CD44$^+$CD4$^+$TCRβ$^+$RORγt$^+$T-bet$^-$], Th1 [live Dump$^-$FOXP3$^-$CD44$^+$CD4$^+$TCRβ$^+$RORγt$^-$T-bet$^+$] and Th2 cells [liveDump$^-$FOXP3$^-$CD44$^+$CD4$^+$TCRβ$^+$RORγt$^-$T-bet$^-$GATA3$^+$].

The stained cells were analyzed using an FACS Fortessa BD flow cytometer or sorted with an FACS Aria II BD cell sorter (BD, Sparks, MD, USA). For scRNA-seq, CD45$^+$ cells isolated from the lungs pooled from two or more mice were used for each replicate.

Adoptive transfer

We pooled lungs from 4 to 6 donor mice and sorted them using flow cytometry. We isolated donor cells from CD45.1$^+$ mice and used recipient mice as CD45.2$^+$ mice. CD39$^+$CD9$^+$ IM (CD45$^+$CD11b$^+$CD11c$^-$Ly6G$^-$CD39$^+$CD9$^+$) donor cells were sorted from OVA + LPS/OVA + αIL-23p19 or PBS/PBS mice on day 24. Moreover, CD39$^+$CD9$^+$ neutrophil (CD45$^+$CD11b$^+$CD11c$^-$Ly6G$^+$ CD39$^+$CD9$^+$) donor cells were sorted from PBS/PBS mice. PBS was also used as a non-cellular negative control. We adoptively transferred 2.5 to 3.5 × 10^4 cells into the recipient mice (OVA + LPS/OVA) via intravenous route four times on 14, 15, 21, and 22 days and then examined the number of the injected cells present in the lung of the recipient CD45.2$^+$ mice under OVA + LPS/OVA on 24 days.

scRNA-seq

We performed scRNA-seq analysis of CD45$^+$ cells isolated from NDA mouse lungs in OVA + LPS/PBS ($n = 3$), OVA + LPS/OVA ($n = 3$), or OVA + LPS/OVA + αIL-23p19 ($n = 3$). CD45$^+$ cells isolated from the lungs pooled from two or more mice were used for each replicate. Cellular suspensions were loaded onto a chromium controller (10X Genomics) to generate nanoliter-sized gel bead-in-emulsions (GEMs) containing single cells, reagents, and a single gel bead containing barcoded oligonucleotides. Barcoded sequencing libraries were prepared using Chromium Next GEM Single Cell 3′ v3.1 Dual Index (10X Genomics) according to the manufacturer's protocol. The sequencing libraries were sequenced on NovaSeq 6000 (Illumina) with the following read lengths: 28 base pairs (bp) for Read 1 (16 bp 10x Barcode + 12 bp UMI), 10 bp for Sample Index (dual), and 90 bp for Read 2. The raw and processed data of scRNA-seq were deposited in the Gene Expression Omnibus (GEO) database (GSE222456).

scRNA-seq data analysis

Illumina BCL files were demultiplexed and converted to FASTQ files using the 'cellranger mkfastq' function in Cell Ranger software (v.6.1.2)[73]. The resulting FASTQ files were used to perform alignment to mouse GRCm38 genome, filtering, and UMI counting, as well as to produce gene-barcode matrices using the 'cellranger count' function. Subsequent data analysis was performed using Seurat (v.4.0.4)[44]. We first selected cells that had a number of genes per cell over 200 and less than 7000, the number of UMIs per cell over 3000 and less than 35,000, and the percent of mitochondrial reads less than 10%. Gene counts for the selected cells were then normalized by the LogNormalize method using the 'NormalizeData' function, and 2000 highly variable genes were identified using the 'FindVariableFeatures' function. Data integration between the samples was performed using the 'IntegrateData' function. Cell-to-cell variation in the number of detected UMIs, mitochondrial contamination, and cell cycle stage was regressed using the 'ScaleData' function. For clustering analysis, linear dimensional reduction was performed on the scaled data using the 'RunPCA' function, and the number of statistically significant principal components (PCs) used for the subsequent analyses was determined using an Elbow plot. Louvain clustering method was then used to cluster the cells using 'FindNeighbors' and 'FindClusters' functions with a resolution of 0.1 (total cell clustering and subclustering of dendritic cell cluster), 0.075 (subclustering of monocyte cluster), 0.15 (subclustering of alveolar macrophage cluster), 0.21 (subclustering of CD11b$^+$ macrophage cluster), or 0.25 (subclustering of neutrophil-like cell cluster). The numbers of subclusters were determined before the plateau to prevent over-clustering in elbow plots for the total within-clusters sum of squares[74] (Supplementary Fig. 7a). Uniform manifold approximation and projection (UMAP), a nonlinear dimensional reduction method, was used to visualize the clustered cells. Transfer of

cell type labels from ImmGen dataset[46] was performed using SingleR[45] with default parameters.

Identification of marker genes significantly upregulated in the individual cell clusters

Using the normalized gene counts for each detected gene, we calculated Z-transformed Wilcoxon's rank-sum statistic values (*Z*-values) between a cell cluster (Group 1) and the other clusters (Group 2; e.g., Cluster 0 versus Clusters 1–10). We then estimated empirical distributions of Z-values for the null hypothesis (i.e., the expression level of a gene is not different between the two groups) by random permutation of the cells in the two groups. Using the estimated empirical distributions, we computed the adjusted *P*-values for the gene. Finally, we identified the genes significantly upregulated in a cluster compared to the other clusters as those that had 1) adjusted *P*-values < 0.01 (total cell clustering) or 0.05 (subclustering), 2) log-fold changes > 0.4 (1.49-fold; total cell clustering) or 0.25 (1.28-fold; subclustering), and 3) median normalized counts of the cells in the cluster larger than those of the cells in the other clusters.

Functional enrichment analysis

To identify cellular processes represented by the genes, we performed an enrichment analysis of gene ontology biological processes (GOBPs) for the genes using DAVID software[75] and then selected the GOBPs with *P*-value < 0.05 and gene count ≥3.

Bulk RNA-sequencing and data analysis

Total RNA was isolated from $CD39^+CD9^+$ IMs ($n = 3$) under OVA + LPS/OVA + αIL-23p19 condition using TRIzol RNA Isolation Reagent (Life technologies, Carlsbad, CA, USA), and purified according to the manufacturer's instructions. The libraries were prepared for 151 bp paired-end sequencing using RNA Prep with Enrichment, (L) Tagmentation (96 Samples) (Illumina). These cDNA libraries were qualified with the Agilent 4200 Tapestation (Agilent) and quantified with the Qubit Flex Fluorometer (Thermo Fisher Scientific) according to the manufacturer's library protocol. Sequencing was performed as paired-end using NovaSeq 6000 (Illumina). For the read sequences from the sequencing, we removed the adapter sequences and the ends of reads less than Phred quality score 20 using cutadapt (v.1.18)[76]. We then mapped the resulting reads to the *Mus musculus* reference genome (GRCm38) using HISAT2 (v.2.2.1)[77]. We filtered out PCR or optical duplicate reads using Picard (v.2.25.5) (https://broadinstitute.github.io/picard/). We counted the remaining reads for gene features (GTF file of GRCm38) using HTSeq (v.0.11.3)[78]. To estimate the fractions of cells belonging to the subclusters of CM and NL in $CD39^+CD9^+$ IMs, we performed deconvolution analysis with CIBERSORTx[50] based on cell type-specific RNA signatures (i.e., marker genes) of these subclusters. We operated the software in absolute mode with S-mode batch correction and 100 permutations, according to the instructions. The raw and processed data of RNA-sequencing were deposited in the Gene Expression Omnibus (GEO) database (GSE222459).

Analysis of RNA expression profiles of asthma patients

We obtained bulk RNA expression profiles of lung tissues collected by bronchial epithelial brushing from asthma patients with severity and blood neutrophil percentage information available [SARP (GSE63142)][79] from the GEO database. We downloaded the normalized $\log_2$-intensities from the GEO database and applied quantile normalization[80] to the normalized $\log_2$-intensities. To identify present probes, a Gaussian mixture model was fitted to the distribution of the normalized $\log_2$-intensities, and the probes with intensities larger than a cutoff, a value in which two Gaussian distributions meet, in more than half of the samples were determined to be present. If two or more present probes corresponded to a gene, we selected a probe with the largest intensities as a representative probe. For each gene with the present probe, we auto-scaled the normalized $\log_2$-intensities. Next, for each sample, we calculated a signature score as the averaged auto-scaled value for marker genes of $TREM2^{high}$ CM. To identify the marker genes for calculating the signature score, we identified the genes significantly upregulated in $TREM2^{high}$ CM compared to all the other $CD45^+$ immune cells (non-$TREM2^{high}$ CM). To this end, using the normalized gene counts for each detected gene, we calculated *Z*-values between $TREM2^{high}$ CM and non-$TREM2^{high}$ CM. We then estimated an empirical null distribution of *Z*-values by random permutation of the cells. Using the estimated empirical null distribution, we computed the adjusted *P*-values for the gene and finally identified the marker genes of $TREM2^{high}$ CM as those that had 1) adjusted *P*-values < 0.01, 2) log-fold changes > 0.41 (1.5-fold), and 3) proportion of non-$TREM2^{high}$ CM cells expressing the gene < 0.25.

Immunofluorescence staining

To identify NETs from lung tissue, the left lobe of the lung was collected as described above and fixed with 4% paraformaldehyde (PFA) for 24 hr. The left lung lobe was paraffin-embedded for staining. For deparaffinization and rehydration, the slides were washed in xylene, subsequently in ethanol at decreasing concentrations (100, 95, 70, and 50%), and finally with PBS. Next, the slides were boiled in 10 mM sodium citrate buffer (pH 6.0) for 20 min at 90 °C for antigen retrieval. The lung tissues were incubated with PBS containing 2% bovine serum albumin (BSA) and 2% donkey serum (Sigma-Aldrich) for 1 hr at room temperature (RT). They were stained with DAKO antibody diluent (Agilent, Carpinteria, CA, USA) including anti-histone H3 (citrulline R2 + R8 + R17) antibody (ab5103, Abcam, Cambridge, UK) (1:100) and anti-MPO antibody (8F4, NOVUSBIO) (1:100) overnight at 4 °C. After washing the slides with PBS, the slides were stained with DAKO diluent including secondary donkey anti-rabbit IgG antibodies conjugated with Alexa Fluor 568 (1:1000) and donkey anti-goat IgG antibodies conjugated with Alexa Fluor 647 (1:1000) for 2 hr in the dark at RT. Finally, the slides were mounted with Fluoroshield containing DAPI (Sigma-Aldrich) and stored at 4 °C[31]. All samples were analyzed and quantified using a Carl-Zeiss confocal microscope LSM 700, and all quantifications were processed using ZEN 2.3 black software (Carl Zeiss, Dresden, Germany).

ex vivo co-culture NETosis assay

Neutrophils were sorted from OVA + LPS/OVA. $CD39^+CD9^+$ IMs were sorted from OVA + LPS/OVA + αIL-23p19 (Fig. 6) or PBS/PBS (Supplementary Fig. 11). $CD39^-CD9^-$ monocytes were sorted from OVA + LPS/OVA + αIL-23p19 using flow cytometry. Neutrophils (1×10^5 cells/well) were seeded and cultured ex vivo for 2 or 15 hr with or without $CD39^+CD9^+$ IMs (1×10^5 cells/well) in Dulbecco's Modified Eagle's Medium (DMEM; Lonza) supplemented with 10% FBS and 1% penicillin/streptomycin (P/S) on chamber slides (Nunc Lab-TEK II 4 Chamber slide system, Sigma-Aldrich) pre-coated with poly D-lysine hydrobromide (Sigma-Aldrich). POM1 (10 μM/well; Tocris Bioscience), anti-CD9 antibody (5 μg/ml; BD), or ATP (100, 1, 0.1, and 0.01 μM/well) were added to the wells simultaneously with $CD39^+CD9^+$ IMs. To identify NETs from ex vivo co-culture slides, the slides were fixed with 10% PFA and permeabilized with 0.5% Triton X-100 after incubation. The slides were performed immunofluorescence staining to examine NETosis as described above. All samples were analyzed and quantified using a Carl-Zeiss confocal microscope LSM 700, and all quantifications were processed using ZEN 2.3 black software (Carl Zeiss).

ex vivo cell-based apoptosis assay

$CD39^+CD9^+$ IMs or $CD39^-CD9^-$ monocytes from PBS/PBS (5×10^4 cells/well) sorted using flow cytometry were seeded and cultured ex vivo in Dulbecco's Modified Eagle's Medium (DMEM; Lonza) on Nunc Lab-TEK II 8 Chamber slide system (Sigma-Aldrich). Recombinant IL-23 (1 μg/ml, R&D Systems) or anti-IL-23 receptor antibody (1 μg/ml, 258010, R&D Systems) was added to the wells simultaneously with $CD39^+CD9^+$ IMs

or $CD39^-CD9^-$ monocytes for 1 hr. For cell-based analysis, the slides were stained using Annexin V-FITC Apoptosis Detection Kit (ab14085, Biovision, CA, USA). The stained slides were fixed with 4% PFA and mounted with Fluoromount aqueous mounting medium (Sigma-Aldrich). All samples were analyzed and quantified using a Carl-Zeiss confocal microscope LSM 700, and all quantifications were processed using ZEN 2.3 black software (Carl Zeiss). For flow-cytometry analysis, the $CD39^+CD9^+$ IMs or $CD39^-CD9^-$ monocytes were stained using Annexin V-FITC Apoptosis Detection Kit according to the manufacturer's protocol. The stained cells were analyzed using a BD FACS Verse II flow cytometer (BD).

Statistical analysis

Comparisons of samples between two groups were processed by an unpaired Student's t test. However, for the comparison of samples among multiple groups, we performed one-way ANOVA with Tukey's post hoc correction. Furthermore, for comparisons of samples among multiple groups defined by two variables (e.g., Mch dose and experimental condition in Fig. 1i, j), we performed two-way ANOVA with Sidak's post hoc correction. The statistical significance cutoff of $P < 0.05$ was used. All statistical analyses were performed using the GraphPad PRISM 8 software (GraphPad, San Diego, CA, USA). For all graphs, data are displayed as mean ± s.e.m. All these pieces of information are indicated in the Figure legends.

Reporting summary

Further information on research design is available in the Nature Portfolio Reporting Summary linked to this article.

Data availability

scRNA-seq and bulk RNA-seq data generated in this study have been deposited in Gene Expression Omnibus (GEO) database under accession codes: GSE222456 (scRNA-seq, https://www.ncbi.nlm.nih.gov/geo/query/acc.cgi?acc=GSE222456) and GSE222459 (bulk RNA-seq, https://www.ncbi.nlm.nih.gov/geo/query/acc.cgi?acc=GSE222459). All data are publicly available as of the date of publication. Previously published bulk RNA expression profiles of asthma patients (SARP cohort) that were reanalyzed here were downloaded from the GEO database (GSE63142, https://www.ncbi.nlm.nih.gov/geo/query/acc.cgi?acc=GSE63142). All other data are available in the article and its Supplementary files or from the corresponding author upon request. Source data are provided in this paper.

References

1. Fanta, C. H. Asthma. *N. Engl. J. Med.* **360**, 1002–1014 (2009).
2. Holgate, S. T. Innate and adaptive immune responses in asthma. *Nat. Med.* **18**, 673–683 (2012).
3. Levy, B. D. et al. Future research directions in Asthma. An NHLBI working group report. *Am. J. Respir. Crit. Care Med.* **192**, 1366–1372 (2015).
4. Kuruvilla, M. E., Lee, F. E. & Lee, G. B. Understanding Asthma phenotypes, endotypes, and mechanisms of disease. *Clin. Rev. Allergy Immunol.* **56**, 219–233 (2019).
5. Douwes, J., Gibson, P., Pekkanen, J. & Pearce, N. Non-eosinophilic asthma: importance and possible mechanisms. *Thorax* **57**, 643–648 (2002).
6. Gibson, P. G. & Foster, P. S. Neutrophilic asthma: welcome back! *Eur. Respir. J.* **54**, 1901846 (2019).
7. Wadhwa, R. et al. Cellular mechanisms underlying steroid-resistant asthma. *Eur. Respir. Rev.* **28**, 190096 (2019).
8. Panettieri, R. A. Jr Neutrophilic and pauci-immune phenotypes in severe Asthma. *Immunol. Allergy Clin. North Am.* **36**, 569–579 (2016).
9. Bruijnzeel, P. L., Uddin, M. & Koenderman, L. Targeting neutrophilic inflammation in severe neutrophilic asthma: can we target the disease-relevant neutrophil phenotype? *J. Leukoc. Biol.* **98**, 549–556 (2015).
10. Plantinga, M. et al. Conventional and monocyte-derived CD11b(+) dendritic cells initiate and maintain T helper 2 cell-mediated immunity to house dust mite allergen. *Immunity* **38**, 322–335 (2013).
11. Soroosh, P. et al. Lung-resident tissue macrophages generate Foxp3+ regulatory T cells and promote airway tolerance. *J. Exp. Med.* **210**, 775–788 (2013).
12. Iezzi, G. et al. CD40-CD40L cross-talk integrates strong antigenic signals and microbial stimuli to induce development of IL-17-producing CD4+ T cells. *Proc. Natl. Acad. Sci. USA* **106**, 876–881 (2009).
13. Huang, G., Wang, Y. & Chi, H. Regulation of TH17 cell differentiation by innate immune signals. *Cell Mol. Immunol.* **9**, 287–295 (2012).
14. Bettelli, E. et al. Reciprocal developmental pathways for the generation of pathogenic effector TH17 and regulatory T cells. *Nature* **441**, 235–238 (2006).
15. Rehnberg, M., Ramnegård, M., Krutrök, N., Yrlid, L. & Jirholt, J. The role of IL-17 in the OVA-LPS driven model of lung inflammation. *Eur. Respir. J.* **46**, PA4010 (2015).
16. McGeachy, M. J. et al. The interleukin 23 receptor is essential for the terminal differentiation of interleukin 17-producing effector T helper cells in vivo. *Nat. Immunol.* **10**, 314–324 (2009).
17. Langrish, C. L. et al. IL-23 drives a pathogenic T cell population that induces autoimmune inflammation. *J. Exp. Med.* **201**, 233–240 (2005).
18. Guan, Q. et al. Targeting IL-23 by employing a p40 peptide-based vaccine ameliorates murine allergic skin and airway inflammation. *Clin. Exp. Allergy* **42**, 1397–1405 (2012).
19. Li, Y. et al. Silencing IL-23 expression by a small hairpin RNA protects against asthma in mice. *Exp. Mol. Med.* **43**, 197–204 (2011).
20. Trevor, J. L. & Deshane, J. S. Refractory asthma: mechanisms, targets, and therapy. *Allergy* **69**, 817–827 (2014).
21. Yipp, B. G. et al. Infection-induced NETosis is a dynamic process involving neutrophil multitasking in vivo. *Nat. Med.* **18**, 1386–1393 (2012).
22. Brinkmann, V. & Zychlinsky, A. Neutrophil extracellular traps: is immunity the second function of chromatin? *J. Cell Biol.* **198**, 773–783 (2012).
23. Caudrillier, A. et al. Platelets induce neutrophil extracellular traps in transfusion-related acute lung injury. *J. Clin. Invest.* **122**, 2661–2671 (2012).
24. Thomas, G. M. et al. Extracellular DNA traps are associated with the pathogenesis of TRALI in humans and mice. *Blood* **119**, 6335–6343 (2012).
25. Delgado-Rizo, V. et al. Neutrophil extracellular traps and its implications in inflammation: An overview. *Front. Immunol.* **8**, 81 (2017).
26. Papayannopoulos, V. Neutrophil extracellular traps in immunity and disease. *Nat. Rev. Immunol.* **18**, 134–147 (2018).
27. Krishnamoorthy, N. et al. Neutrophil cytoplasts induce TH17 differentiation and skew inflammation toward neutrophilia in severe asthma. *Sci. Immunol.* **3**, eaao4747 (2018).
28. Wright, T. K. et al. Neutrophil extracellular traps are associated with inflammation in chronic airway disease. *Respirology* **21**, 467–475 (2016).
29. Lachowicz-Scroggins, M. E. et al. Extracellular DNA, neutrophil extracellular traps, and inflammasome activation in severe asthma. *Am. J. Respir. Crit. Care Med.* **199**, 1076–1085 (2019).
30. Toussaint, M. et al. Host DNA released by NETosis promotes rhinovirus-induced type-2 allergic asthma exacerbation. *Nat. Med.* **23**, 681–691 (2017).
31. Radermecker, C. et al. Locally instructed CXCR4(hi) neutrophils trigger environment-driven allergic asthma through the release of neutrophil extracellular traps. *Nat. Immunol.* **20**, 1444–1455 (2019).

32. Nabhan, A. N., Brownfield, D. G., Harbury, P. B., Krasnow, M. A. & Desai, T. J. Single-cell Wnt signaling niches maintain stemness of alveolar type 2 cells. *Science* **359**, 1118–1123 (2018).
33. Zepp, J. A. et al. Distinct mesenchymal lineages and niches promote epithelial self-renewal and myofibrogenesis in the lung. *Cell* **170**, 1134–1148.e1110 (2017).
34. Montoro, D. T. et al. A revised airway epithelial hierarchy includes CFTR-expressing ionocytes. *Nature* **560**, 319–324 (2018).
35. Plasschaert, L. W. et al. A single-cell atlas of the airway epithelium reveals the CFTR-rich pulmonary ionocyte. *Nature* **560**, 377–381 (2018).
36. Franks, T. J. et al. Resident cellular components of the human lung: current knowledge and goals for research on cell phenotyping and function. *Proc. Am. Thorac. Soc.* **5**, 763–766 (2008).
37. Treutlein, B. et al. Reconstructing lineage hierarchies of the distal lung epithelium using single-cell RNA-seq. *Nature* **509**, 371–375 (2014).
38. Yu, Y. et al. Single-cell RNA-seq identifies a PD-1(hi) ILC progenitor and defines its development pathway. *Nature* **539**, 102–106 (2016).
39. Guo, M. et al. Single cell RNA analysis identifies cellular heterogeneity and adaptive responses of the lung at birth. *Nat. Commun.* **10**, 37 (2019).
40. Wallrapp, A. et al. The neuropeptide NMU amplifies ILC2-driven allergic lung inflammation. *Nature* **549**, 351–356 (2017).
41. Kim, H. K. et al. PI3Kδ contributes to ER stress-associated asthma through ER-redox disturbances: the involvement of the RIDD-RIG-I-NF-κB axis. *Exp. Mol. Med.* **50**, e444 (2018).
42. Namakanova, O. A. et al. Therapeutic potential of combining IL-6 and TNF blockade in a mouse model of allergic asthma. *Int. J. Mol. Sci.* **23**, 3521 (2022).
43. Bachus, H. et al. Impaired tumor-necrosis-factor-α-driven dendritic cell activation limits lipopolysaccharide-induced protection from allergic inflammation in infants. *Immunity* **50**, 225–240 (2019).
44. Stuart, T. et al. Comprehensive integration of single-cell data. *Cell* **177**, 1888–1902 (2019).
45. Aran, D. et al. Reference-based analysis of lung single-cell sequencing reveals a transitional profibrotic macrophage. *Nat. Immunol.* **20**, 163–172 (2019).
46. Heng, T. S. & Painter, M. W. The immunological genome project: networks of gene expression in immune cells. *Nat. Immunol.* **9**, 1091–1094 (2008).
47. Niessen, N. M. et al. Neutrophilic asthma features increased airway classical monocytes. *Clin. Exp. Allergy* **51**, 305–317 (2021).
48. Tippett, E., Cameron, P. U., Marsh, M. & Crowe, S. M. Characterization of tetraspanins CD9, CD53, CD63, and CD81 in monocytes and macrophages in HIV-1 infection. *J. Leukoc. Biol.* **93**, 913–920 (2013).
49. Antonioli, L., Pacher, P., Vizi, E. S. & Haskó, G. CD39 and CD73 in immunity and inflammation. *Trends Mol. Med.* **19**, 355–367 (2013).
50. Newman, A. M. et al. Determining cell type abundance and expression from bulk tissues with digital cytometry. *Nat. Biotechnol.* **37**, 773–782 (2019).
51. Kawano, H. et al. IL-10-producing lung interstitial macrophages prevent neutrophilic asthma. *Int. Immunol.* **28**, 489–501 (2016).
52. Yadav, V. et al. Ectonucleotidase tri(di)phosphohydrolase-1 (ENTPD-1) disrupts inflammasome/interleukin 1beta-driven venous thrombosis. *J. Clin. Invest.* **129**, 2872–2877 (2019).
53. Di Domizio, J. & Gilliet, M. Psoriasis caught in the NET. *J. Invest. Dermatol.* **139**, 1426–1429 (2019).
54. Lande, R. et al. Neutrophils activate plasmacytoid dendritic cells by releasing self-DNA-peptide complexes in systemic lupus erythematosus. *Sci. Transl. Med.* **3**, 73ra19 (2011).
55. Chen, X., Li, Y., Qin, L., He, R. & Hu, C. Neutrophil extracellular trapping network promotes the pathogenesis of neutrophil-associated asthma through macrophages. *Immunol. Invest.* **50**, 544–561 (2021).
56. Nakajima, H. & Hirose, K. Role of IL-23 and Th17 cells in airway inflammation in asthma. *Immune Netw.* **10**, 1–4 (2010).
57. Mangan, S. & Alon, U. Structure and function of the feed-forward loop network motif. *Proc. Natl. Acad. Sci. USA* **100**, 11980–11985 (2003).
58. Brightling, C. E., Nair, P., Cousins, D. J., Louis, R. & Singh, D. Risankizumab in severe asthma - A phase 2a, placebo-controlled trial. *N. Engl. J. Med.* **385**, 1669–1679 (2021).
59. Fabre, T. et al. Identification of a broadly fibrogenic macrophage subset induced by type 3 inflammation. *Sci. Immunol.* **8**, eadd8945 (2023).
60. Schoenborn, J. R. & Wilson, C. B. Regulation of interferon-gamma during innate and adaptive immune responses. *Adv. Immunol.* **96**, 41–101 (2007).
61. Yu, M. et al. Identification of an IFN-γ/mast cell axis in a mouse model of chronic asthma. *J. Clin. Invest.* **121**, 3133–3143 (2011).
62. Taube, C. et al. Transient neutrophil infiltration after allergen challenge is dependent on specific antibodies and Fc gamma III receptors. *J. Immunol.* **170**, 4301–4309 (2003).
63. Newcomb, D. C. et al. Estrogen and progesterone decrease let-7f microRNA expression and increase IL-23/IL-23 receptor signaling and IL-17A production in patients with severe asthma. *J. Allergy Clin. Immunol.* **136**, 1025–1034 (2015).
64. Lajoie, S. et al. Complement-mediated regulation of the IL-17A axis is a central genetic determinant of the severity of experimental allergic asthma. *Nat. Immunol.* **11**, 928–935 (2010).
65. Nakagome, K. et al. High expression of IL-22 suppresses antigen-induced immune responses and eosinophilic airway inflammation via an IL-10-associated mechanism. *J. Immunol.* **187**, 5077–5089 (2011).
66. Maltby, S., Tay, H. L., Yang, M. & Foster, P. S. Mouse models of severe asthma: Understanding the mechanisms of steroid resistance, tissue remodelling and disease exacerbation. *Respirology* **22**, 874–885 (2017).
67. Aun, M. V., Bonamichi-Santos, R., Arantes-Costa, F. M., Kalil, J. & Giavina-Bianchi, P. Animal models of asthma: utility and limitations. *J. Asthma Allergy* **10**, 293–301 (2017).
68. Yu, Q. L. & Chen, Z. Establishment of different experimental asthma models in mice. *Exp. Ther. Med.* **15**, 2492–2498 (2018).
69. Xu, H. et al. Exosomal microRNA-21 derived from bronchial epithelial cells is involved in aberrant epithelium-fibroblast cross-talk in COPD induced by cigarette smoking. *Theranostics* **8**, 5419–5433 (2018).
70. McGovern, T. K., Robichaud, A., Fereydoonzad, L., Schuessler, T. F. & Martin, J. G. Evaluation of respiratory system mechanics in mice using the forced oscillation technique. *J. Vis. Exp.* e50172 https://doi.org/10.3791/50172 (2013).
71. Wang, N. et al. Neutrophil extracellular traps induced by VP1 contribute to pulmonary edema during EV71 infection. *Cell Death Discov.* **5**, 111 (2019).
72. Lu, Y. et al. Expansion of CD4(+) CD25(+) and CD25(-) T-Bet, GATA-3, Foxp3 and RORγt cells in allergic inflammation, local lung distribution and chemokine gene expression. *PLoS ONE* **6**, e19889 (2011).
73. Zheng, G. X. et al. Massively parallel digital transcriptional profiling of single cells. *Nat. Commun.* **8**, 14049 (2017).
74. Zhang, H. et al. A multitask clustering approach for single-cell RNA-seq analysis in Recessive Dystrophic Epidermolysis Bullosa. *PLoS Comput. Biol.* **14**, e1006053 (2018).
75. Huang da, W., Sherman, B. T. & Lempicki, R. A. Systematic and integrative analysis of large gene lists using DAVID bioinformatics resources. *Nat. Protoc.* **4**, 44–57 (2009).

76. Martin, M. Cutadapt removes adapter sequences from high-throughput sequencing reads. *EMBnet J.* **17**, https://doi.org/10.14806/ej.17.1.200 (2011).
77. Kim, D., Paggi, J. M., Park, C., Bennett, C. & Salzberg, S. L. Graph-based genome alignment and genotyping with HISAT2 and HISAT-genotype. *Nat. Biotechnol.* **37**, 907–915 (2019).
78. Anders, S., Pyl, P. T. & Huber, W. HTSeq–a Python framework to work with high-throughput sequencing data. *Bioinformatics* **31**, 166–169 (2015).
79. Modena, B. D. et al. Gene expression in relation to exhaled nitric oxide identifies novel asthma phenotypes with unique biomolecular pathways. *Am. J. Respir. Crit. Care Med.* **190**, 1363–1372 (2014).
80. Bolstad, B. M., Irizarry, R. A., Astrand, M. & Speed, T. P. A comparison of normalization methods for high density oligonucleotide array data based on variance and bias. *Bioinformatics* **19**, 185–193 (2003).

Acknowledgements

This work was supported by the Bio & Medical Technology Development Program of the National Research Foundation of Korea (NRF), funded by the Ministry of Science, ICT & Future Planning (2019M3A9B6066971 to J.-H.R., 2022M3A9F3017506 to J.-H.R., and 2022M3A9F3094557 to J.-H.R.), (2019M3A9B6066960 to D.H.), and the Korea Mouse Phenotyping Project (2016M3A9D5A01952415 to J.-H.R.). This study was supported by a faculty research grant from Yonsei University College of Medicine (6-2017-0075 to J.-H.R.). We would like to thank Heon Yung Gee (Yonsei University, Korea) for microscopy imaging assistance; Ho-Keun Kwon (Yonsei University, Korea) for technical support with FACS sorting; and Tae-Gyun Kim (Yonsei University, Korea) for helpful comments and suggestions during this work.

Author contributions

J.-H.R., D.H., and J.-H.Y. conceptualized the study, designed the experiments, and wrote the manuscript. S.H. performed experiments and analyzed the data with assistance from B.K., D.J., J.R., B.-R.K., S.C.P., S.J.S., and J.-Y.L. D.Y.H., D.H., Y.H.C., and J.K.K. analyzed the scRNA-seq data. J.-S.N., H.-J.C., C.-H.K., J.P., J.H.C., S.W.L., T.-B.K., and Y.W.C. assisted with the study design. All authors read and commented on the manuscript.

Competing interests

The authors declare no competing interests

Additional information

Supplementary information The online version contains supplementary material available at https://doi.org/10.1038/s41467-024-53038-2.

Correspondence and requests for materials should be addressed to Joo-Heon Yoon, Daehee Hwang or Ji-Hwan Ryu.

Peer review information *Nature Communications* thanks the anonymous reviewer(s) for their contribution to the peer review of this work. A peer review file is available.